

# 1 Mapping seasonal glacier melt across the Hindu Kush Himalaya with time series SAR

2 Corey Scher<sup>1,2</sup>, Nicholas C. Steiner<sup>2</sup>, Kyle C. McDonald<sup>1,2,3</sup>

3 <sup>1</sup>Department of Earth and Environmental Science, The Graduate Center, City University of New York, New York,  
4 10031, United States

5  
6 <sup>2</sup>Department of Earth and Atmospheric Science, The City College of New York, City University of New York, New  
7 York, 10031, United States

8  
9 <sup>3</sup>Carbon Cycle and Ecosystems Group, Jet Propulsion Laboratory, California Institute of Technology. 4800 Oak  
10 Grove Drive, Pasadena. CA 91001, USA

11 *Correspondence to:* Nicholas C. Steiner (nsteiner@ccny.cuny.edu)

12 **Abstract.** Current observational data on Hindu Kush Himalayas (HKH) glaciers are sparse, and characterizations  
13 of seasonal melt dynamics are limited. Time series synthetic aperture radar (SAR) imagery enables detection of  
14 reach-scale glacier melt characteristics across continents. We analyze C-band Sentinel-1 A/B SAR time series data,  
15 comprised of 32,741 Sentinel-1 A/B SAR images, determine the duration of seasonal glacier melting for 105,432  
16 mapped glaciers (83,102 km<sup>2</sup> glacierized area), defined using optical observations, in the HKH across the calendar  
17 years 2017-2019. Melt onset and duration are recorded at 90m spatial resolution and 12-day temporal repeat. All  
18 glacier areas within the HKH exhibit some degree of melt. Melt signals persist for over half of the year at elevations  
19 below 4,000 m a.s.l. and for nearly one quarter of the calendar year at elevations exceeding 7,000 m a.s.l. Retrievals  
20 of seasonal melting span all elevation ranges of glacierized area in the HKH region, extending greater than 1km  
21 above the maximum elevation of an interpolated 0°C summer isotherm and at the top of Mount Everest, where *in*  
22 *situ* data and surface energy balance models indicate the Khumbu glacier is melting at surface air temperatures  
23 below -10°C. Sentinel-1 melt retrievals reflect broad-scale trends in glacier mass balance across the region where the  
24 duration of melt retrieved in the Western Himalaya and Karakoram is on average one month less than in the Eastern  
25 Himalaya sub-region. Furthermore, percolation zones are apparent from meltwater retention indicated by delayed  
26 refreeze. Time series SAR datasets are suitable to support operational monitoring of glacier surface melt and the  
27 development and assessment of surface energy balance models of melt-driven ablation across the global cryosphere.

## 28 1 Introduction

29 Global warming driven by the anthropogenic release of geologic carbon is causing mass wasting of alpine  
30 glaciers worldwide (Brangers et al.; Zemp et al., 2006). The Hindu Kush Himalaya (HKH) region, known  
31 colloquially as the “Third Pole,” has the most ice-covered area on Earth after the high-latitude polar regions (Yao et  
32 al., 2012). In contrast to large ice sheets near the poles, these relatively small alpine glaciers – perched at some of  
33 the highest elevations on Earth – are among the most sensitive indicators within the global cryosphere of changes in  
34 global climate (Anthwal et al., 2006). Just as the recession of these sensitive mountain ice caps contributes to over  
35 one quarter of global sea level rise (Zemp et al., 2019), disturbances accompanying HKH glacier retreat pose  
36 innumerable hazards to humans and natural ecosystems. Glacier retreat threatens to disturb the dynamics of river

37 systems delivering freshwater resources to nearly 2 billion people across South and Central Asia (Brown et al.,  
38 2007; Milner et al., 2017). Outburst floods resulting from glacier mass wasting have killed at least 6,300 people in  
39 the Himalayas alone, and have caused extensive damage to property and livelihoods. These outbursts are expected to  
40 increase in frequency with continued glacier wasting (Carrivick and Tweed, 2016). Some organisms endemic to  
41 alpine aquatic ecosystems may become extinct as they lose biogeochemical regulation from upstream glaciers  
42 (Jacobsen et al., 2012). As global temperatures rise and perennial snow and ice cover decreases, societies are faced  
43 with difficult decisions around the costs and benefits of adapting to a changing climate within and around the HKH  
44 region (Brown et al., 2007). Informed decision-making for successful climate change adaptation will require  
45 knowledge of the state of natural systems and how these systems are projected to change alongside future increases  
46 in population and global average temperature (Bogardi et al., 2012).

47 Substantial uncertainties exist in the current understanding of projected disturbances associated with a  
48 changing climate, environment, and hydrologic regime across the greater Himalayas due to a lack of observations of  
49 hydrology and meteorology at high elevations (Litt et al., 2019). The magnitude and rate of ablation from surface  
50 melting is of particular importance as it drives changes in accumulation-zone snow-properties, such as percolation  
51 and densification, that feedback into increased melting (Alexander et al., 2019). Surface melting has also been  
52 linked to increased englacial temperatures resulting in faster ice motion (Miles et al., 2018). Although the general  
53 trajectory of changes to the HKH cryosphere is understood (i.e. accelerated glacier mass loss on a decadal scale in  
54 the Central and Eastern Himalaya), a consensus in projecting changes to HKH hydrology is lacking largely because  
55 of missing *in situ* snow and ice monitoring data across these glaciated river basins (Fujita and Nuimura, 2011).  
56 However, construction and maintenance of *in situ* monitoring station networks is costly and labor-intensive because  
57 of the complexity of the high-mountain glaciated terrain. Satellite imaging radar retrieval of alpine glacier melt  
58 characteristics has long been proposed as a source of data for hydrologic and glaciologic research (Shi et al., 1994).  
59 Understanding of surface melting from observation records will enable advanced climate change projections of  
60 glacier wasting that require snow property dynamics describing the retention, refreezing and drainage of liquid water  
61 within glacier snow and firn (Pritchard et al., 2020).

62 Recent findings indicate that shortwave radiation drives melting at elevations where air temperatures are  
63 perennially below freezing, such as those on Mount Everest where temperatures never exceed -10°C (Matthews et  
64 al., 2019; Matthews et al., 2020). These *in situ* findings indicate the degree to which temperature-indexed melt  
65 models are underestimating ablation at these elevations using a 0°C threshold for glacier melting. Further, studies of  
66 glacier wasting in High Mountain Asia have shown variability in patterns and magnitude of glacier wasting across  
67 sub-regions of the HKH that would be difficult to capture in numerical models using degree-day assumptions (Brun  
68 et al., 2017). An observationally based dataset providing characteristics of the glacier surface energy balance is  
69 necessary to capture seasonal and regional variability in glacier wasting across the HKH during melt-freeze cycles.

70

## 71 **1.1 Snowmelt Detection and Radar Imaging**

72 This study builds on extensive research on microwave scattering from dry and wet snow and associated  
73 techniques for snowmelt retrieval from imaging radar data to present an operational monitor for spatially-resolved  
74 glacier surface melt characteristics using synthetic aperture radar (SAR) time series and outlines of glacier area  
75 derived from satellite optical imagery across the HKH. Microwave remote sensing has been used to reliably monitor  
76 melt patterns across glaciers and ice sheets (Abdalati and Steffen, 2001; Ashcraft and Long, 2007; Jezek et al.,  
77 1994b; Steiner and Tedesco, 2014). Because imaging radar is independent of solar illumination and largely  
78 unaffected by cloud cover and atmospheric conditions, the fidelity of radar observations is defined by the frequency  
79 of the satellite platform's observational opportunities and by the characteristics of the imaging sensor. At C-band  
80 frequencies, frozen glacier percolation areas are recognized as one of the brightest radar targets on Earth, and glacier  
81 surfaces are unambiguous targets for determination of surface melt/freeze characteristics (Jezek et al., 1994; Rott  
82 and Mätzler, 1987). Detection of seasonal melt on ice surfaces at C-Band frequencies (4 – 8 GHz) depends on a  
83 strong radiometric response at melt onset (MO), when liquid water content introduced to an otherwise frozen snow  
84 or firn matrix causes a drastic decrease in the radar backscatter from the medium (Hallikainen et al., 1986). Deep,  
85 frozen snow and firn has a high scattering albedo across microwave frequencies (Matzler, 1998), resulting in high  
86 radar backscatter intensity over glaciated regions during the frozen months (Winsvold et al., 2018; Wiscombe and  
87 Warren, 1980). The introduction of liquid water in the snow or firn matrix at even hydrologically minimal amounts  
88 causes a pronounced increase in the medium's dielectric constant, increasing radar signal attenuation and  
89 diminishing volume scattering, and leading to a pronounced decrease in radar backscatter, usually by half power or  
90 more (Kendra et al., 1998; Shi and Dozier, 1995). In areas that are seasonally snow-free, *e.g.* for glacier ablation  
91 areas of debris-cover or bare ice, melting conditions are dominated by heterogeneous scattering mechanisms  
92 following the disappearance of seasonal snow, a topic of study not well represented in the theoretical literature on  
93 radar physics likely due to the complex nature of the glacier ablation surface. Because of the relatively strong signal  
94 produced at the onset of melting, radar-based melt-detection records have been developed across regions of the  
95 global cryosphere for several decades using both real and synthetic aperture radar sensors (Bhattacharya et al., 2009;  
96 Bindshadler et al., 1987; Koskinen et al., 1997). Subsequently, snowmelt detection algorithms have been developed  
97 using a host of radar sensors to monitor the onset and duration of snowmelt across glaciers and ice sheets (Abdalati  
98 and Steffen, 2001; Ashcraft and Long, 2007; Bahr et al., 1997; Jezek et al., 1994; Kayastha et al., 2019; Koskinen et  
99 al., 1997; Winebrenner et al., 1994). Prior applications of SAR mapping of seasonal surface melting over ice sheets  
100 and glaciers have been limited by a lack of repeat observations such as those now available from the Sentinel-1 SAR  
101 constellation (Lund et al., 2019).

102 Observations from time series SAR data have been used to delineate zones of glacier facies and regions of  
103 glacier mass balance (Winsvold et al., 2018). In glacier percolation zones, seasonally wet snow refreezes into ice  
104 lenses, pipes, and other percolation-related features that amplify both surface and volume scattering of C-band radar  
105 and result in the brightest SAR backscatter being captured during the frozen periods (Jezek et al., 1994; Rau et al.,  
106 2000). Studies have shown that SAR backscatter generally increases with elevation across glacier surfaces during  
107 frozen periods, from the glacier terminus, through frozen meltwater percolation zones, and eventually attenuating in

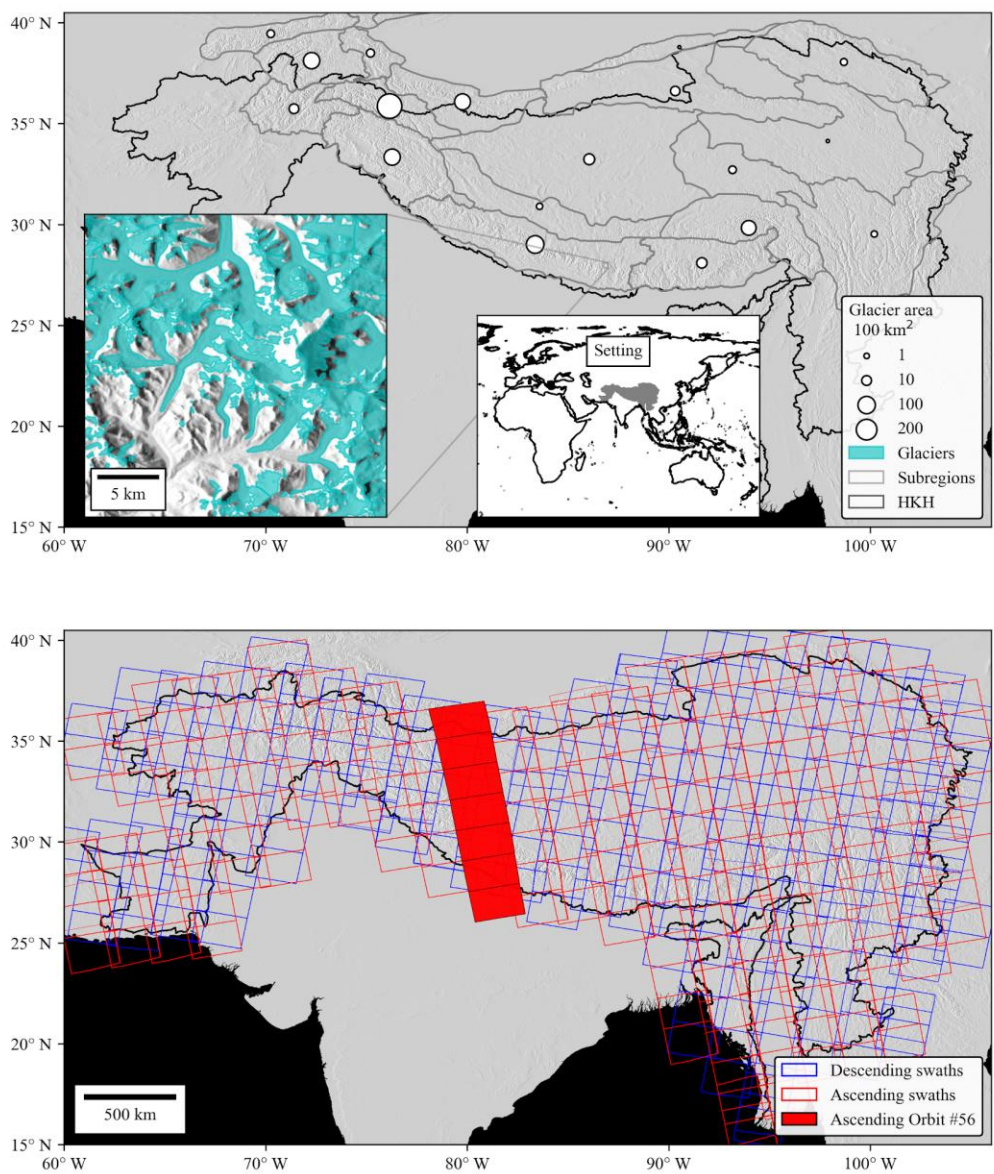
108 zones where dry snow accumulates (Winsvold et al., 2018). In transitions between these zones there are pronounced  
109 backscatter contrasts rather than smooth, gradual transitions. At C-band frequencies, radar scattering within glacier  
110 percolation areas dominates the backscatter amplitude during frozen periods (Jezek et al., 1994). Importantly for  
111 melt retrievals, the diminished volume scattering during surface melting in areas of meltwater percolation creates a  
112 pronounced and unambiguous radar signature in time-series observations. The sensitivity of SAR backscatter to the  
113 introduction of liquid water in an otherwise frozen snowpack or firn structure provides a reliable mechanism for the  
114 retrieval of percolation zone melt characteristics (Lievens et al., 2019). In refreezing percolation zones, the upper  
115 layers of firn will freeze first with the freezing front advancing downward across layers, thus progressively increasing  
116 backscatter and with decreasing total-column liquid water content (Ashcraft and Long, 2005). In this way, the timing  
117 of refreeze relative to the surface energy balance at the surface provides a direct and spatially resolved indicator of  
118 subsurface meltwater storage within the snow or firn and delineates the percolation zones over mountain glaciers.

119 This study enlists SAR data acquired at a spatiotemporal resolution that captures melt variability across  
120 mountain glacier surfaces suitable for constraining seasonal characteristics of melt onset and duration while building  
121 on associated methods often employed for glaciers and ice sheets. In this paper we utilize SAR data to retrieve melt  
122 status on HKH glacier surfaces with a simple threshold-based change detection classification melt/freeze state - an  
123 observational constraint on the surface energy balance. It is likely that intense incident solar radiation is driving  
124 these melt processes at elevations above the 0°C summer isotherm (Matthews et al., 2019) across the entirety of the  
125 HKH, and that the sensitivity of SAR backscatter to changes in the glacier surface melt/freeze condition as seen  
126 when water transitions between solid and liquid phases provides a real alternative to temperature elevation lapse rate  
127 estimates of melting (Litt et al., 2019) for assessing surface energy balance models of glacier ablation. Though  
128 coarse in temporal resolution relative to typical meteorological datasets, retrieval of melt status using SAR time  
129 series produces mappings with very high spatial resolution and a continuous record of melt timing and duration  
130 across glaciated regions. We present an application of this melt retrieval technique at the scale of the HKH with  
131 spatiotemporal fidelity adequate to capture seasonal variability in melt timing and duration across individual glacier  
132 surfaces and capture sub-regional heterogeneities across the HKH.

## 133 **2 Setting and Data**

134 The HKH region (*Fig. 1*) spans 13 million km<sup>2</sup>, including areas inhabited by 240 million people with nearly  
135 2 billion people relying on the delivery of water resources from catchments that originate within the region (Scott et  
136 al., 2019). Within the high elevation HKH, seasonal meltwater from snow and glacier ice is the primary source of  
137 domestic freshwater supply (Bolch et al., 2012). Wasting of HKH glaciers poses a risk to the domestic water  
138 resources supply for those populations living within these high elevation HKH catchments (Wood et al., 2020).  
139 Glacier wasting in the HKH is heterogeneous; increases in global average temperature have caused wasting of  
140 mountain glaciers across all HKH sub-regions, save the eastern Karakoram, Kunlun Shan, and adjacent sub-regions  
141 at the intersection of South and Central Asia (Gardelle et al., 2012). Distinct glacio-climatic sub-regions are  
142 characterized by these unique dynamics of glacier wasting (Bolch et al., 2019a). The wasting of HKH glaciers is  
143 thus a spatially and temporally heterogeneous phenomenon where distinct glacio-climatic regimes control ablation

144 (Bolch et al., 2012). In this study, we refer to glacio-climate sub-regions delineated in Bolch, et al. (2019a) and  
 145 modified by Shean, et al. (2020). These delineations of glacio-climate were produced by the Hindu Kush Himalaya  
 146 Monitoring and Assessment Program (HiMAP) and we will refer to the sub-regional delineations as “HiMAP  
 147 regions” throughout the text. We selected 17 HiMAP subregions that intersected with a boundary of the HKH region  
 148 delineated by the International Center for Integrated Mountain Development (ICIMOD). The HKH region, HiMAP  
 149 sub-regions, and glaciated area summaries within each HiMAP sub-region are illustrated in *Fig. 1* alongside  
 150 Sentinel-1 acquisition plan.



151  
 152 **Figure 1. (Top)** Hindu Kush Himalaya (HKH) region and 2018 GAMDAM glacierized areas summed across  
 153 glacio-climate sub-regions from Shean, et al. (2020). An inset map highlights the spatial fidelity of GAMDAM  
 154 outlines in the top panel. GGI and HKH data overlay a 30m Shuttle Radar Topography Mission (SRTM) DEM  
 155 hillshade (Farr, 2007a). **(Bottom)** Sentinel-1 ascending (red) and descending (blue) swath footprints acquired across  
 156 the study region. Ascending orbit cycle number 56 is highlighted in red to illustrate the SAR image processing  
 157 approach for time series analysis across distinct orbit cycles.

## 158 2.1 GAMDAM Glacier inventory (GGI)

159 The Glacier Area Mapping for Discharge from the Asian Mountains (GAMDAM) glacier inventory (GGI) is  
160 a contemporary (July 2019) database on glacier outlines for the region of High Mountain Asia (*Fig. 1*). These  
161 outlines were originally delineated automatically using cloud and snow-free satellite optical imagery in an initial  
162 release of the database (Nuimura et al., 2015). As a recent update to the database, each outline was individually  
163 inspected for quality control to correct discrepancies where automatic glacier delineation lost accuracy in terrain-  
164 occluded areas, at debris covered portions of glaciers, and through obstruction under seasonal snowpack. The  
165 recently updated glacier outlines were derived from satellite optical imagery captured across the HKH by Landsat 5  
166 and 7 between 1990-2010 (Sakai, 2019). Although these data are the most current in terms of quality control  
167 spanning the study region, they do not necessarily capture debris-covered portions of glaciers due to confusion with  
168 land in optical image classification schemes; an issue that may be resolved with interferometric SAR phase  
169 decorrelation (Bolch et al., 2019b). The 2018 GAMDAM database contained within the HiMAP sub-regions  
170 includes 105,432 distinct glacier outlines spanning a total area of 83,102 km<sup>2</sup> within the HKH (Nuimura et al.,  
171 2015).

## 172 2.2 Sentinel-1 Synthetic Aperture Radar

173 The Sentinel-1 A/B satellites were launched in April of 2014 and 2016, respectively, and collect C-band  
174 (5.405 GHz) SAR data with a combined revisit interval of 6-days over of the majority of the terrestrial Earth. Each  
175 Sentinel-1 scene acquired in the interferometric wide-swath (IW) mode has a width of 250 km and a resolution of  
176 5x20 meters in range and azimuth at the equator. This study utilized images taken in the IW mode and in cross-  
177 polarized state (VH). Sentinel-1 data were accessed through a cloud-computing platform (discussed below) wherein  
178 SAR scenes were radiometrically terrain corrected to backscatter intensity values in decibels (dB) using the  
179 European Space Agency's (ESA) Sentinel Application Platform (SNAP) toolbox and the Shuttle Radar Topography  
180 Mission (SRTM) 30m digital elevation model (DEM) (Farr, 2007) upon ingestion into the cloud environment. Data  
181 from both the ascending and descending orbit nodes were analyzed across the study region for a total consideration  
182 of 32,741 individual Sentinel-1 A/B IW scenes across 46 unique orbit cycles captured across the calendar years  
183 2017-2019 (*Table 1, Fig. 1b*). By combining orbit directions, we utilize observations acquired at day and night. For  
184 the purpose of this study we do not attempt to resolve diurnal-scale melt-freeze processes and instead focus on  
185 retrieving seasonal and annual characteristics of melt timing and duration. Cross-polarized SAR backscatter  
186 provides enhanced observational sensitivity to volume scattering of the radar signal in deep, dense and weathered  
187 snowpack and firn (Rott and Mätzler, 1987). We selected cross-polarized (VH) Sentinel-1 A/B observations because  
188 VH data show less angular sensitivities to contrasts between dry and wet snow (Nagler et al., 2016). Cross-polarized  
189 Sentinel-1 SAR did not become available over the HKH until early 2017 and thus restricted this study timeframe. As  
190 illustrated in *Fig. 2*, we observe a large (>3dB) difference in the seasonal radar backscatter between frozen and  
191 melting conditions across the entirety of glacier surfaces in cross-polarized (VH) SAR data.

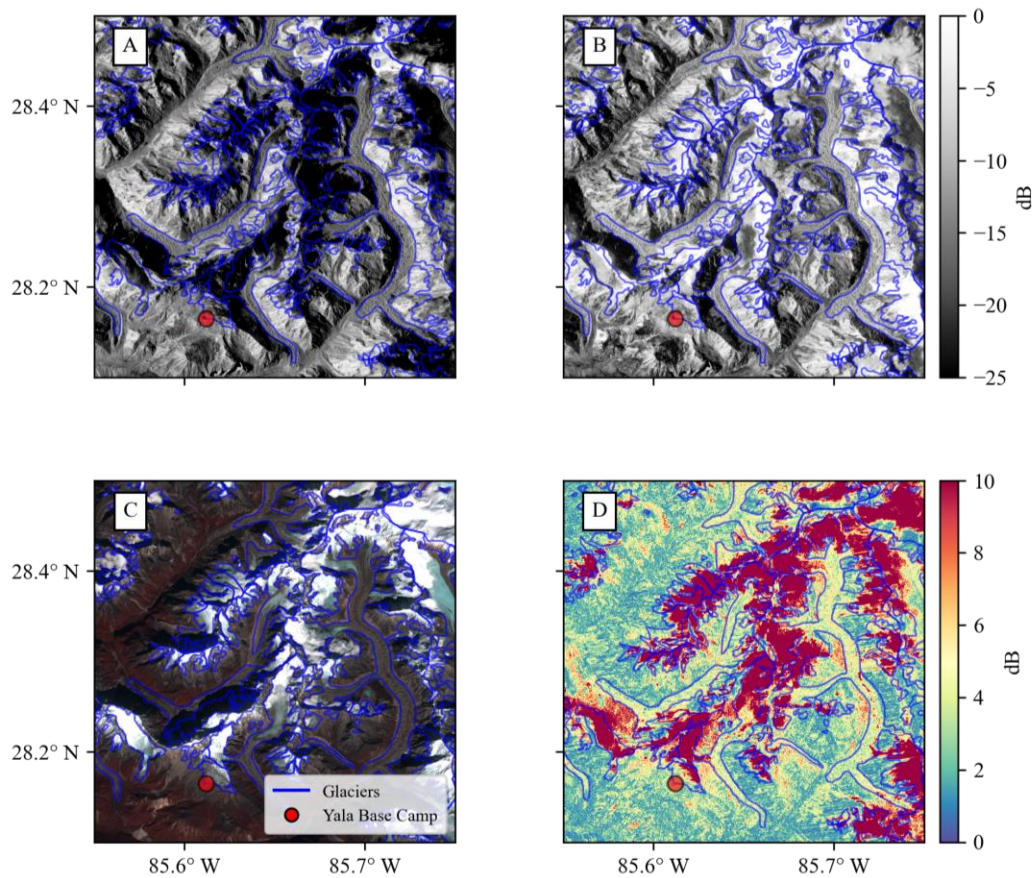
192



193 **Table 1.** Sentinel-1 image count and orbit paths used in this study.

| Orbit Direction | Number of S-1 Images by Year |       |       | Relative orbit cycle   |
|-----------------|------------------------------|-------|-------|--|
|                 | 2017                         | 2018  | 2019  |  |
| Descending      | 4,424                        | 5,436 | 5,253 | 4, 5, 19, 20, 33, 34, 48, 49, 62, 63, 77, 78, 92, 106, 107, 121, 122, 135, 136, 150, 151, 164, 165   |
| Ascending       | 5,302                        | 6,097 | 6,150 | 12, 13, 26, 27, 41, 42, 55, 56, 70, 71, 85, 86, 99, 100, 114, 115, 128, 129, 143, 144, 158, 172, 173 |

194



195  
196  
197  
198  
199  
200  
201  
202

**Figure 2.** (A) Mean summer (July-August) 2018 cross-polarized (VH) backscatter across an example region in the Trishuli basin, Nepal. (B) Mean 2018 winter (January- February) VH backscatter from Sentinel-1. (C) Sentinel-2 false-color (near-infrared, green, blue) image acquired by Sentinel-2 on October 30, 2018. Glacier outlines are shown in blue and the Yala glacier base camp meteorological station is marked in red. Note the snow covered and bare-ice portions of outlined glaciers and other debris-covered portions of glacier ablation areas. (D) The difference between mean summer and winter VH backscatter from Sentinel-1.

### 203 2.3 Computing Infrastructure

204 A cloud-computing platform and application programming interface with pre-processed radiometrically  
205 terrain corrected Sentinel-1 A/B data was used to detect melt characteristics across the region (Gorelick et al., 2017).

206 Radiometric terrain correction of Sentinel-1 data was conducted upon ingestion to the cloud server using the ESA’s  
 207 method contained within the Sentinel Applications Platform (SNAP) processing toolbox. The SNAP toolbox is used  
 208 for Sentinel-1 images to update orbit metadata with restituted orbit files, remove invalid edge data and low intensity  
 209 noise, remove thermal noise, compute  $\sigma^0$  backscatter, and conduct orthorectification upon ingestion of data to the  
 210 server (Google, 2020). The SNAP toolbox terrain correction functionality utilizes the 30m spatial resolution SRTM  
 211 DEM (Farr, 2007; Margulis et al., 2019). The pre-processed SAR times series data and API functionality used to  
 212 derive glacier melting characteristics are available from Google Earth Engine and can be used to recreate the work  
 213 presented in this study.

## 214 **2.4 Automated Weather Station Data**

215 Measurements from two automated weather stations (AWS) are used to estimate surface energy balance (SEB)  
 216 and evaluate surface melting conditions over high elevation glaciers. The Camp II (27.9810°N, 86.9023°E, 6,464 m  
 217 a.s.l.) and the South Col (27.9719°N, 86.9295°E, 7,945 m a.s.l.) AWS were installed around Mount Everest, Nepal as  
 218 part of the National Geographic and Rolex Perpetual Planet Expedition to Mt. Everest in April-May 2019 (Matthews  
 219 et al., 2019). Measurements were collected at an hourly interval and include air temperature, wind speed, relative  
 220 humidity, incoming shortwave and longwave radiation and barometric pressure. Time series plots of meteorological  
 221 observations are shown in *Supplementary Information Fig. S1*. Please see Matthews et al. (2020) for a complete  
 222 description of sensor specifications and sampling interval.

## 223 **3 Methods**

### 224 **3.1 Melt Classification**

225 We use a threshold-based change detection algorithm applied to time series radar backscatter intensity to  
 226 classify melt conditions (Ashcraft and Long, 2007). Melt detection is conducted across Sentinel-1 A/B ascending  
 227 and descending orbit track time series separately and mosaicked into a final image based on a statistical score for  
 228 seasonal melt magnitude after classification. To classify snowmelt, we conduct a pixel-based temporal classification  
 229 by comparing each image at interval  $i$  to a dry/frozen winter average backscatter value calculated from January to  
 230 February for each study year. Due to missing VH acquisitions at some locations during the 2017 frozen months, (Jan  
 231 – Feb) we utilized 2018 frozen month reference data for melt retrieval across the calendar year 2017, as regular  
 232 acquisitions across the HKH began in late February 2017. Snowmelt at each image acquisition interval ( $m_i$ ) was  
 233 classified using *Eq. (1)*:

$$234$$

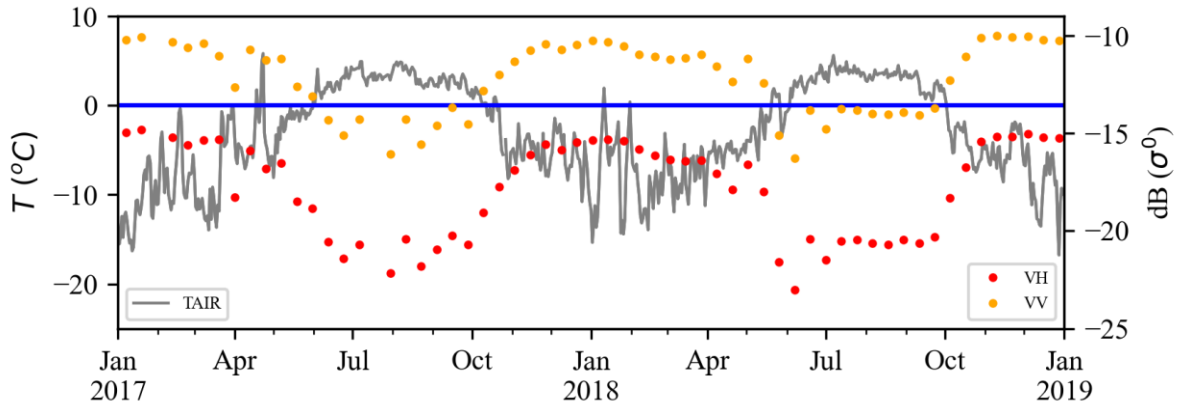
$$235 \quad m_i = \begin{cases} 1, & \text{if } \sigma^0_i < \bar{\sigma}^0_w - b, \\ 0, & \text{if } \sigma^0_i > \bar{\sigma}^0_w - b. \end{cases} \quad (1)$$

$$236$$

237 where the ground-range detected backscatter intensity at each image acquisition ( $\sigma^0_i$ ) within the times series must  
 238 be less than the difference between the mean winter backscatter ( $\bar{\sigma}^0_w$ ) and a fixed threshold ( $b$ ). Threshold values



239 (b) have been developed across numerous studies of melt detection with C-band scatterometer and SAR datasets  
 240 using both ground-based observations and radar scattering model results of changes to backscatter magnitude at the  
 241 onset of melt. We followed previous studies (Baghdadi et al., 1997; Bhattacharya et al., 2009; Engeset et al., 2002;  
 242 Nagler and Rott, 2000; Oza et al., 2011; Rott and Mätzler, 1987; Steiner and Tedesco, 2014; Trusel et al., 2012) and  
 243 selected a  $b$  value equal to one half of the signal power (-3 dB). *Figure 3* provides an illustration of the SAR melt  
 244 signal for a high elevation (4,950m a.s.l) meteorological station, located at the Yala glacier base camp. Backscatter  
 245 values averaged across the Yala glacier acquired along the Sentinel-1 A/B descending orbit direction are plotted  
 246 alongside mean daily air temperature recorded at the Yala glacier base camp automatic weather station (Shea, 2016).  
 247 If we consider air temperature above 0°C to control glacier surface melt at this location, classification accuracy for  
 248 melt retrieval using *Eq. (1)* is 96% in the VH polarization.



249 **Figure 3.** Time-series chart of air temperature measured at the Yala glacier base camp (4,950 m a.s.l) and Sentinel-1  
 250 A/B descending backscatter averaged across the Yala glacier for the years 2017-2018. Assessment of algorithm  
 251 performance assuming mean daily air temperatures above 0°C indicates active melt results in 96% accuracy for melt  
 252 classification across this time series in the VH polarized backscatter.  
 253

### 254 3.2 Quantifying algorithm performance

255 Sentinel-1 SAR viewing geometry will vary as the local incidence angle increases with across-track range. At  
 256 high incidence angles (far range), the sensitivity to volume scatter is diminished and the melting signal is reduced.  
 257 At C-band frequencies, these effects on volume scatter are strongest only at very high incidence angles (closer to  
 258 grazing) (Nagler and Rott, 2000). We classified areas as valid for melt detection using a metric of statistical  
 259 separability for seasonal backscatter intensity across frozen and melt periods, which we interpret as a measure of the  
 260 strength of the seasonal melt signal *Eq. (2)*:

$$261 \quad z = \frac{\bar{\sigma}_w^0 - \bar{\sigma}_s^0}{s(\sigma_w^0)}, \quad (2)$$

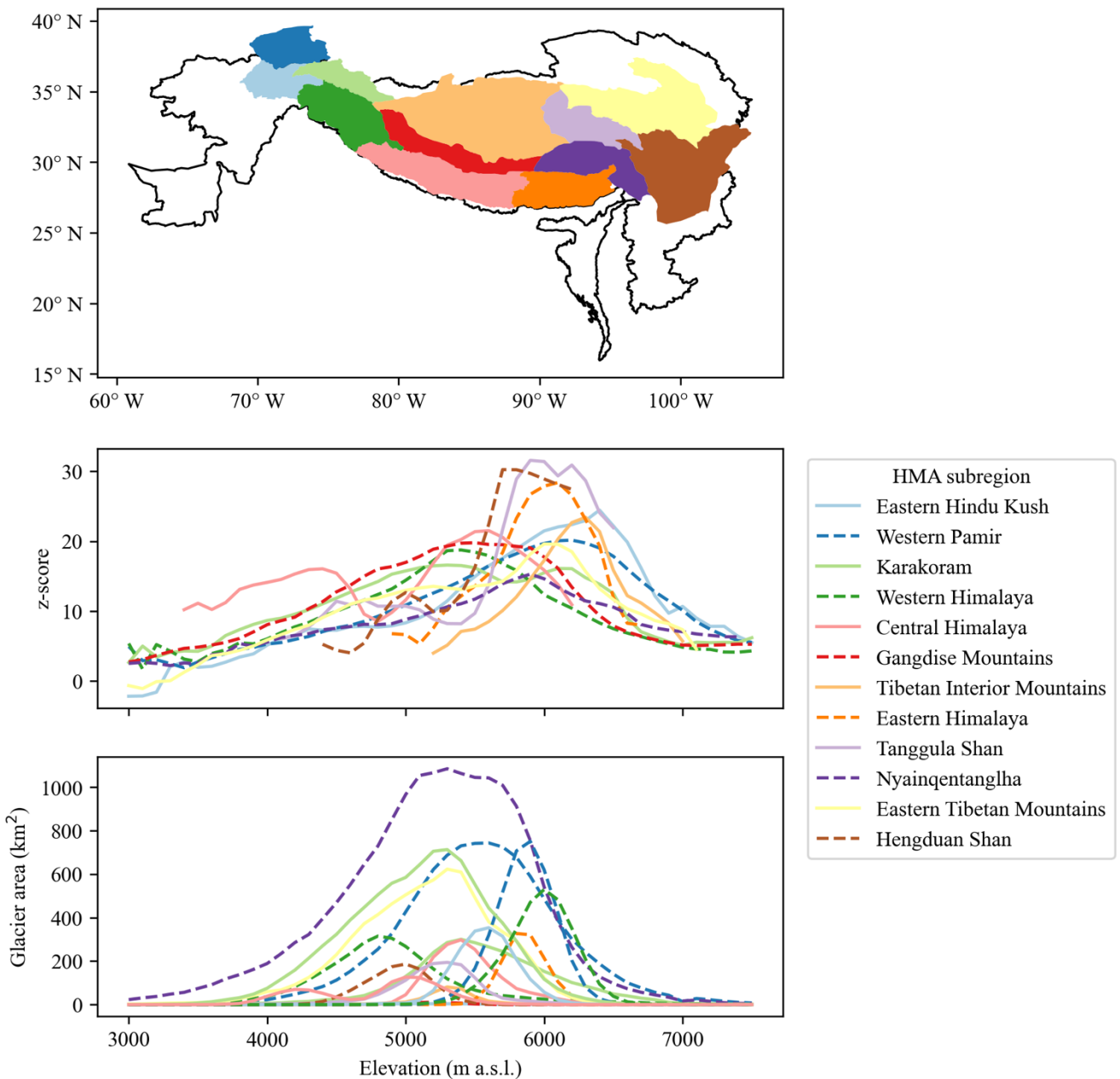
262 where the score for seasonal separability of backscatter intensity ( $z$ ) was calculated across each SAR pixel's time  
 263 series using the difference between the mean winter  $\bar{\sigma}_w^0$  (January-February) and summer  $\bar{\sigma}_s^0$  (July-August) season  
 264 backscatter intensities, as compared to the standard deviation of backscatter across the winter months  $s(\sigma_w^0)$ . In  
 265  
 266

267 computing  $z$ , we employed consistent repeat-pass observation geometries thereby allowing application of the time  
268 series melt-detection algorithm in regions of complex terrain. This metric serves as a measure of the magnitude of  
269 the seasonal melt signal across each pixel's time series. It is used here as a criterion to identify valid melt  
270 observations and for selection of pixels employed in regions of overlapping orbital tracks, based on the sensitivity of  
271 the radar backscatter to melting. We apply this metric to choose which orbit direction (ascending or descending) to  
272 use for melt classification on a per-pixel basis after applying *Eq. (1)* across each orbit cycle time series, so as to  
273 capture the maximum area of melt signals occurring across the complex terrain.

274 Sentinel-1 A/B interferometric wide (IW) swath images have a range in viewing angle between 29.1–46.0°  
275 (ESA). Glacier melt retrieval using SAR data commonly begins with a normalization of radar images by viewing  
276 angle on a scene by scene basis (Adam et al., 1997; Huang et al., 2011; Rott and Mätzler, 1987; Winsvold et al.,  
277 2018). We consider changes for each individual orthorectified 10x10m pixel time series across distinct, repeating  
278 orbit tracks and directions. This approach holds the local incidence angle effectively constant for each region  
279 observed by a given set of orbit tracks. Glacier melt classification and  $z$ -score calculation are carried out across  
280 images acquired along identical orbit tracks in distinct orbit directions (*Fig. 1*) and mosaicked into a final dataset for  
281 each study year using the greatest  $z$ -score observed across each orbit cycle path and in each orbit direction. We thus  
282 limit temporal resolution of melt retrievals to 12-days by choosing only observations from the orbit direction with  
283 the greater  $z$ -score on a per-pixel basis. Time series analysis of SAR acquisitions on distinct orbit tracks eliminates  
284 the need to normalize each scene by incidence angle for the purposes of melt retrieval. This method reduces  
285 computational cost and eliminates artefacts that may originate from overlapping orbit paths and differences in radar  
286 viewing angle. Areas where complex topography controls the backscatter should show little time series variability in  
287 backscatter change at the SAR pixel scale when viewed at a distinct and consistent orbit path and direction and  
288 should not pass the  $z$  score test.

289 We apply time series melt detection only where inter-seasonal backscatter intensities are separated by  
290 greater than two standard deviations ( $z > 2$ ), representing better than 98% confidence in the presence of an annual  
291 melt signal. For all locations, the orbit direction and orbit cycle that has the greatest  $z$  value is used for melt  
292 classification. We find that  $z$  generally increases with elevation across sub-regions of the HKH and that, across  
293 elevation ranges, the mean  $z$  is above the threshold for melt retrieval, indicating detection of a seasonal melt signal  
294 across all ranges of glacier elevation spanning the HKH (*Fig. 4*). Areas of debris-cover may exhibit radar  
295 brightening with snow-free conditions above winter mean ( $z < 0$ ). These areas occur towards lower elevations  
296 where seasonal snow, or firn, does not have significant contribution to the seasonal backscatter response and are not  
297 included in our melt classification approach following  $z$ -score thresholding. Nonetheless, there exists retrievable  
298 melt signals (i.e.  $z > 2$ ) across ablation surfaces such that median window filtering across ablation zones can result  
299 in a geospatial dataset with more complete coverage. We obtain more robust estimates of melting onset and refreeze  
300 by spatially aggregating results of the glacier surface melt timing (*Eq. 1*) using a median window filter of 9x9 pixels  
301 after melt classification and  $z$ -score validation. Reach-scale regions where SAR signals fail the  $z$ -score test are thus  
302 interpolated over using 9x9 pixel median window filtering. The complexity of SAR signals involves the diverse  
303 scattering mechanisms on ablation surfaces following the disappearance of seasonal snow. Because sufficient data is

304 retrievable on ablation surfaces (i.e.  $z > 2$ ), median window filtering enables greater spatial continuity in SAR-  
 305 derived melt retrieval data. All spatiotemporal characteristics we report herein are after median window filtering of  
 306 melt retrievals from 10m native resolution to 90m resolution. In *Fig. 4* we show the mean  $z$  across HiMAP sub-  
 307 regions in order to illustrate that, on average, even where debris-covered portions of glaciers may exhibit an inverse  
 308 response to melt with the disappearance of snow, Sentinel-1 records a mean  $z$  indicative of a seasonal snowmelt  
 309 signal across all elevation ranges of glaciation. Mean seasonal melt magnitude averaged over 100m elevation bins  
 310 over all three calendar years of data shows strong ( $z > 2$ ) melt signals across glacio-climatic sub-regions and across  
 311 all elevation ranges of significant glaciation (*Fig. 4*).



312 **Figure 4. (Top)** Glacio-climate sub-regions within the Hindu Kush Himalaya codified in Shean, et al. (2020).  
 313 **(Middle)** Mean z-score (2017-2019) by 100m SRTM elevation bin over each sub-region in the HKH. **(Bottom)**  
 314

315 Mapped glacier area from the GAMDAM database (Sakai, 2019) over 100m SRTM (Farr, 2007) elevation bins for  
316 each sub-region.

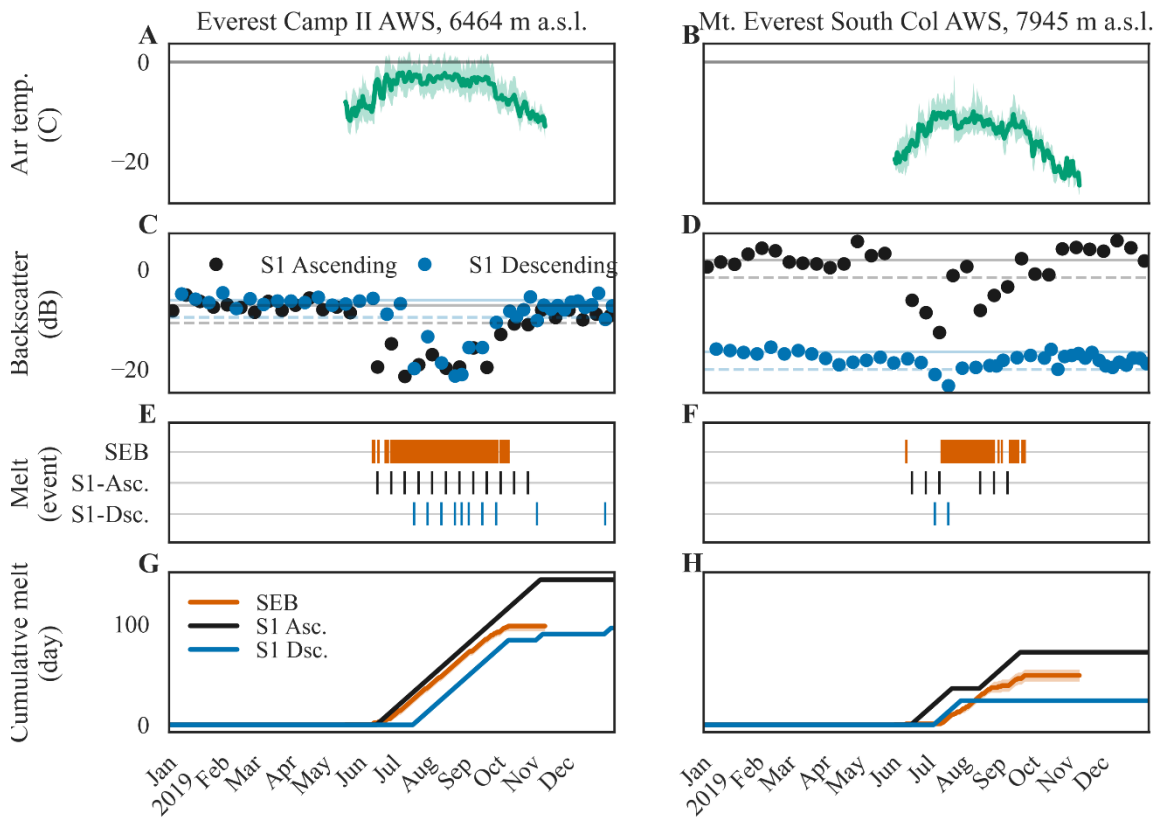
### 317 **3.3 Surface Energy Balance and Surface Melting**

318 Sentinel-1 SAR (S1-SAR) detects a substantial area and duration of melting at elevations where air  
319 temperatures should be well below freezing. Although measurement data in these areas are scarce, AWS installed  
320 during 2019 at Mt Everest Nepal can provide two instances of point-scale validations of glacier melting using  
321 surface energy balance (SEB) modelling based on *in situ* measurements. As described in Matthews et al. (2020), the  
322 highest AWS on the Earth are installed adjacent to the Khumbu Glacier, Nepal. We use AWS observations to  
323 compute SEB described in Matthews et al. (2020). In our SEB modelling, turbulent fluxes are determined using the  
324 aerodynamic roughness at the glacier surface taken from measurements in low latitudes (Brock et al., 2006) and  
325 evaluated over the 5<sup>th</sup> to 95<sup>th</sup> percentile of this sample to capture uncertainty. Surface melting is defined by the  
326 glacier surface temperature ( $T_s$ ) that is evolved from air temperature ( $T_a$ ) and the residual downward glacier heat  
327 flux in the iterative approach from Wheler and Flowers (2011). Melting days are defined where  $T_s = 0^\circ C$  at any  
328 point during the day. Supplementary information for this paper is provided to describe the SEB methodology in  
329 further detail (*Supplementary Information Section SI.1*).

330 A comparison of S1-SAR and SEB derived melting is shown in *Fig. 5*. During 2019, maximum daily  $T_a$   
331 measurements at the Camp II station (*Fig. 5A*) reach above-zero temperatures starting June 13<sup>th</sup> and ending on  
332 September 11<sup>th</sup>. The maximum  $T_s$  reaches  $0^\circ C$  starting on June 2<sup>nd</sup> and ending on September 27<sup>th</sup>. At the South Col  
333 AWS, the average temperature is much less, where maximum temperatures are never above melting and close to -  
334  $10^\circ C$  on average during summer months (*Fig. 5B*). S1-SAR estimates of surface melting use two aggregated  
335 backscatter time-series over 90m x 90m areas where area centers are located nearest to each of the AWS stations  
336 over the Khumbu glacier, Nepal. For the Camp II AWS, this is centered at 6,483 m a.s.l. and for the South Col  
337 AWS, 7,128 m a.s.l. Melting signals are apparent at both Camp II (*Fig. 5C*) and South Col (*Fig. 5D*). A more robust  
338 comparison would match the timings of satellite overpasses and meteorological observations and acknowledge that  
339 some disagreement between melting estimates is resultant from this difference.

340 Melting is detected at high elevations in both SAR observations and SEB modelling output where daily  
341 average air temperatures remain below zero. We find that S1 and SEB estimates of surface melting at the Everest  
342 Camp II AWS (6,464 m a.s.l.) have an agreement score, the percentage of days where the SEB and SAR find the  
343 same condition, that ranges from 73% to 85% depending on the parameterization of surface roughness used in SEB  
344 estimates of melting. At Mt. Everest South Col (7,945 m a.s.l.) the agreement score varies from 63 to 68 percent.  
345 The S1-SAR record indicates 133 days of melting at Camp II while the SEB indicates from 93 to 100 days. At Mt.  
346 Everest South Col AWS the S1-SAR record indicates 72 days of melting while the SEB indicates 43 to 56. The start  
347 of surface melting at Camp II from SEB modeling is day of year (DOY) 153 and DOY 142 from S1-SAR, at South  
348 Col melt onset is DOY 152 from SEB and DOY 146 from S1-SAR. The end of surface melting at Camp II from  
349 SEB modeling is DOY 270 and DOY 290 from S1-SAR. At South Col, refreeze at the surface from SEB is DOY  
350 256 and DOY 244 from S1-SAR.

351 Using SEB outputs we find good agreement on surface melt timings, S1-SAR detects melt onset to within 9  
 352 days on average at two locations on the Khumbu Glacier in Nepal and refreeze to within 16 days. Although limited  
 353 by observational data, the agreement in melt duration between S1-SAR and SEB modeling and the understanding of  
 354 the physical basis of SAR measurements we have a high degree of confidence in our methodology and in the ability  
 355 of the SAR backscatter to detect melting-and in data-poor regions such as HMA.  
 356



357 **Figure 5.** Average daily air temperature measurements, with maximum and minimum (shaded) from (A) the Everest  
 358 Camp II automated weather station (AWS) and (B) the Mt. Everest South Col AWS are compared to glacier surface  
 359 melting observations from the Sentinel-1 satellite synthetic aperture radar (SAR). (C) The radar backscatter from the  
 360 Khumbu Glacier (at 6,483 m a.s.l.) adjacent to the Camp II AWS, show a pronounced decrease in backscatter over  
 361 several months associated with on-going surface melting during summer months. Melting is identified when  
 362 backscatter decreases below a threshold (dashed-line), set at 3 dB below the winter mean (solid-line). (D) At the  
 363 upper reaches of the Khumbu Glacier (7,128 m a.s.l.), S1-SAR observes melting during ascending passes (18:00  
 364 local time) but not during descending passes (06:00 local time) except for a brief period during late June., (F)  
 365 Timing of surface melt from observation and SEB modeling are compared to S1 ascending and descending  
 366 observations at (E) Camp II and (F) South Col AWS. The cumulative number of melting days from the SEB model  
 367 and S1-SAR are shown for (G) Camp II and (H) South Col.  
 368

### 369 3.3 Comparison to temperature elevation lapse rates

370 Melting on glacier surfaces across the HKH is controlled by the SEB between the atmosphere and  
 371 underlying snow, firn or ice. We explore the relationship between the S1-SAR derived surface melting record and

372 air temperature-elevation lapse rates within the Central Himalayas during 2018 using data from two meteorological  
 373 stations within the Langtang Valley (*Table 2*). Temperature-elevation lapse rates were determined using three-day  
 374 averages of hourly air temperature measurements interpolated to fill gaps using methods identical for the calculation  
 375 of temperature elevation lapse rates in numerical model studies of snowmelt and glacier wasting in the HKH (Baral  
 376 et al., 2014). We calculated the difference between three-day average air temperatures and divided by the difference  
 377 in elevation (1,148 m) between the two stations in the Langtang River Valley, Nepal. Lapse-rates ranged from 5°C  
 378 km<sup>-1</sup> in July of 2018 to -13.7°C km<sup>-1</sup> in December of the same year. Temperature-elevation lapse rates were used to  
 379 extrapolate the maximum elevation of three isotherms (-10°C, -5°C, and 0°C) for each day of year in 2018 in order to  
 380 compare extrapolated temperatures with melt retrievals from Sentinel-1.

381  
 382 **Table 2.** Sources of air temperature data used to calculate 3-day average temperature-elevation lapse rates within the  
 383 Central Himalaya for the 2018 calendar year.

| STATION NAME     | DATE RANGE (DD/MM/YYYY) | RESOLUTION | ELEVATION (M A.S.L.) | LATITUDE | LONGITUDE | SOURCE |
|------------------|-------------------------|------------|----------------------|----------|-----------|--------|
| YALA GLACIER     | 05/08/2012 – 12/31/2018 | Hourly     | 4,950                | 28.23252 | 85.61208  | ICIMOD |
| KYANGING STATION | 03/22/2012 – 12/31/2019 | Hourly     | 3,802                | 28.21081 | 85.56169  | ICIMOD |

384

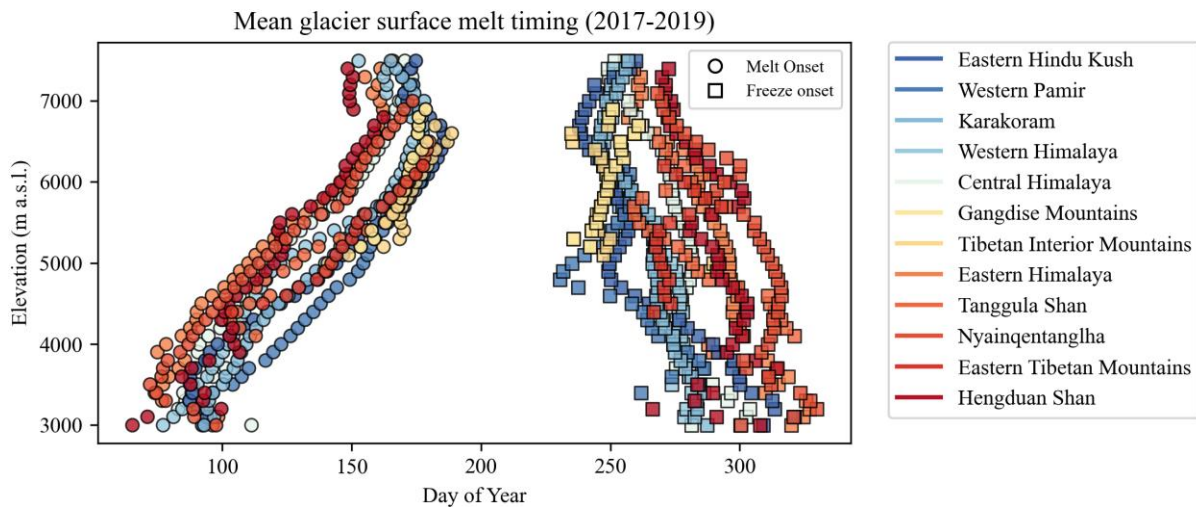
#### 385 4 Results and Discussion

386 A melting signal ( $z > 2$ ) is observed across all mapped glacier area contained in the GAMDAM inventory.  
 387 Melt retrievals are aggregated across 17 glacio-climate sub-regions within the HKH delineated within the HiMAP  
 388 dataset (Shean et al., 2020) and averaged across the calendar years 2017-2019 to report summary statistics (*Table 3*).  
 389 Aggregate statistics of melt onset (MO) and freeze onset (FO) are calculated across 100m elevation bins using the  
 390 30m SRTM (Farr, 2007) digital elevation model for each glacio-climate sub-region as presented in *Figure 4*. For all  
 391 sub-regions, there is a roughly linear relationship of mean MO with elevation over most ranges in elevation. The  
 392 progression of MO with increasing elevation is consistent with lapse rate temperature controls on surface melting for  
 393 most elevation ranges. Notably, we find an inflection toward earlier melt onset occurring at higher elevations  
 394 (>6,500 m a.s.l.). A divergence from lapse-rate driven melting at high elevations suggests that snowmelt onset may  
 395 have regional triggers, like strong solar insolation (Matthews et al., 2019) or variable regional weather patterns; such  
 396 as increases in atmospheric moisture, cloudiness, and deep convection (Lau et al., 2010).

397 In the three years of freeze onset (FO) across sub-regions we do not find the level of elevation dependence  
 398 as observed in MO (*Fig. 6*). For much of the HKH, FO occurs during a short period of time and over large spans of  
 399 elevation. For example, in the Central Himalaya sub-region, FO has a range of 33 days while the MO for this region  
 400 spans 79 days on average. FO across sub-regions does not follow a linear trend with elevation similar to MO (*Fig.*  
 401 *6*). In western sub-regions (Eastern Hindu Kush, Western Pamir, and Karakoram), there is a signal of delayed  
 402 refreeze apparent in summary statistics at higher elevation ranges within each respective catchment. In the Western  
 403 Pamir, FO at 6,000 m occurs 22 days later than FO at 5,000m a.s.l (*Supplementary Fig. S2*). Similarly, in the

404 Karakoram, FO occurs 10 days later at 7,500 m a.s.l. compared to 6,500 m a.s.l. In the Tanggula Shan, FO at 6,500  
405 m a.s.l. is delayed by 21 days relative to FO at 5,500 m a.s.l.

406 Signals of delayed refreeze are observed at elevation ranges similar to greatest  $z$ -score across each sub-  
407 region. Complete refreeze across the depth of a percolation zone is delayed relative to percolation zone surfaces  
408 because liquid water is retained within a percolation zone media after the surface of the percolation zone has frozen  
409 (Paterson, 2016). Completely frozen percolation zones produce some of the largest radar backscatter responses on  
410 the terrestrial earth (Jezek et al., 1994). Because frozen snow and percolation facies are essentially transparent, C-  
411 band SAR will be sensitive to the presence of liquid water across the volume of a snowpack or firn strata (Fischer et  
412 al., 2019). Signals of delayed refreeze across sub-regions are indicative of meltwater storage within the percolation  
413 volume due to meltwater retention. A figure illustrating melt timings and  $z$ -score metric is included as  
414 Supplementary materials (*Supplementary Fig. S2*).



415  
416 **Figure 6.** Mean melt onset (MO) and freeze onset (FO) summarized in 100m elevation bins using the 30m SRTM  
417 digital elevation model (Farr, 2007) and 12 HiMAP sub-regions (Shean, 2020). The blue to red color scale indicates  
418 the longitude of the HiMAP region centroid, where the westernmost regions are shown in dark blue and easternmost  
419 shown in dark red.  
420



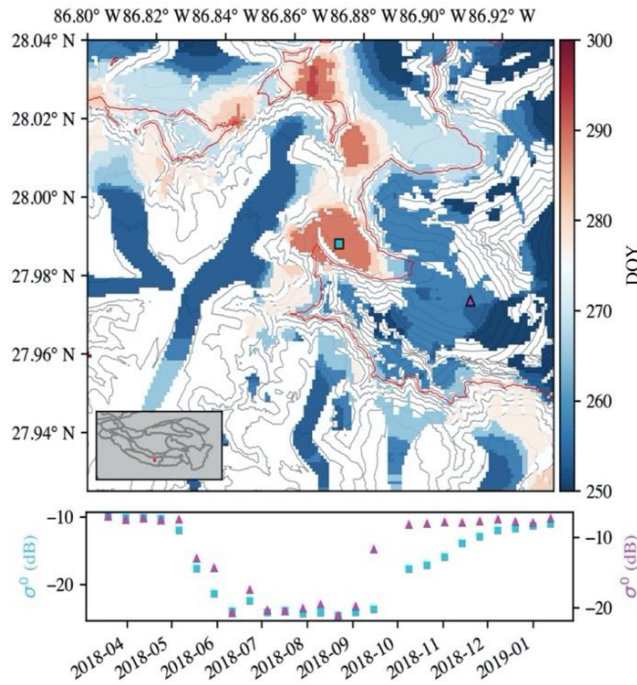
421 **Table 3.** Melt retrieval statistics summarized across HiMAP sub-regions and aggregated over 1km elevation bins  
 422 from the SRTM 30m DEM. Data for each elevation bin and sub-region are structured where the first row is the melt  
 423 onset (MO) in day of year (DOY) and associated MO variance in days, freeze onset (DOY) and associated variance  
 424 (days), and the area of melt retrieved in units of square kilometers.

| <i>Elevation Range (m a.s.l.)</i> | <i>Western Pamir</i> | <i>Western Himalaya</i> | <i>Tibetan Interior</i> | <i>Tanggula Shan</i> | <i>Nyainqentanglha</i> | <i>Karakoram</i> | <i>Hengduan Shan</i> | <i>Gangdise</i> | <i>Eastern Tibetan</i> | <i>Eastern Hindu Kush</i> | <i>Eastern Himalaya</i> | <i>Central Himalaya</i> |
|-----------------------------------|----------------------|-------------------------|-------------------------|----------------------|------------------------|------------------|----------------------|-----------------|------------------------|---------------------------|-------------------------|-------------------------|
| 3000-3999                         | 117 (20)             | 94 (9)                  | -                       | -                    | 79 (19)                | 105 (19)         | 90 (27)              | -               | -                      | 101 (13)                  | 75 (17)                 | 90 (21)                 |
|                                   | 275 (28)             | 280 (22)                | -                       | -                    | 300 (38)               | 278 (23)         | 294 (39)             | -               | -                      | 276 (42)                  | 293 (46)                | 277 (22)                |
|                                   | 602                  | 156                     | -                       | -                    | 145                    | 955              | 11                   | -               | -                      | 89                        | 25                      | 49                      |
| 4000 - 4999                       | 141 (16)             | 113 (14)                | 136 (1)                 | 120 (13)             | 105 (13)               | 128 (20)         | 113 (17)             | -               | 136 (10)               | 131 (17)                  | 102 (20)                | 104 (17)                |
|                                   | 255 (23)             | 275 (15)                | 299 (11)                | 290 (14)             | 310 (18)               | 268 (19)         | 294 (21)             | -               | 268 (12)               | 257 (27)                  | 292 (24)                | 274 (14)                |
|                                   | 5271                 | 3651                    | <1                      | 17                   | 2637                   | 5889             | 231                  | -               | 26                     | 2179                      | 353                     | 1492                    |
| 5000 - 5999                       | 159 (12)             | 138 (20)                | 166 (11)                | 161 (13)             | 131 (18)               | 152 (15)         | 121 (24)             | 164 (14)        | 151 (10)               | 152 (12)                  | 129 (18)                | 134 (20)                |
|                                   | 250 (16)             | 263 (22)                | 249 (14)                | 265 (20)             | 302 (24)               | 262 (19)         | 289 (24)             | 247 (11)        | 275 (15)               | 253 (16)                  | 290 (20)                | 274 (17)                |
|                                   | 4103                 | 6135                    | 3109                    | 2184                 | 5253                   | 15060            | 1245                 | 1123            | 381                    | 1333                      | 2621                    | 7374                    |
| 6000 - 6999                       | 177 (13)             | 163 (11)                | 172 (12)                | 169 (9)              | 150 (11)               | 170 (17)         | 146 (15)             | 166 (10)        | 173 (7)                | 180 (13)                  | 152 (13)                | 156 (12)                |
|                                   | 243 (12)             | 247 (13)                | 249 (12)                | 284 (29)             | 294 (22)               | 249 (13)         | 289 (16)             | 250 (9)         | 280 (5)                | 243 (10)                  | 279 (18)                | 268 (15)                |
|                                   | 117                  | 357                     | 1634                    | 112                  | 295                    | 2752             | 43                   | 438             | 4                      | 177                       | 774                     | 2303                    |
| 7000 - 7999                       | 170 (9)              | 162 (18)                | -                       | -                    | 167 (9)                | 171 (20)         | 151 (5)              | 177(-)          | -                      | 175 (20)                  | 161 (12)                | 169 (13)                |
|                                   | 249 (8)              | 250 (10)                | -                       | -                    | 269 (4)                | 248 (12)         | 269 (7)              | 258(-)          | -                      | 243 (13)                  | 260 (12)                | 249 (14)                |
|                                   | 2                    | 13                      | -                       | -                    | 1                      | 110              | 1                    | <1              | -                      | 11                        | 22                      | 153                     |

425

## 426 4.1 Percolation Meltwater Hydrology

427 Delayed freeze-up apparent in summary statistics at unique elevation ranges across glacio-climate sub-  
428 regions is an important illustration of how melt retrievals from Sentinel-1 are sensitive to the presence of liquid  
429 water within the snowpack and/or firn subsurface (Brangers et al.; Fischer et al., 2019). At the Khumbu glacier on  
430 Mount Everest, Sentinel-1 retrieved refreeze occurs over thirty days later at ~6,000m a.s.l. compared to elevations  
431 below 5,400m a.s.l. and above 6,200m a.s.l., indicating that liquid meltwater was retained at elevation ranges  
432 between ~5,400-6,200m a.s.l. during a month when elevations both above and below this range were recorded as  
433 completely frozen within Sentinel-1 retrieved melt signals. The time series of mean Sentinel-1 SAR backscatter for  
434 descending orbital nodes from two 250m buffered points on the Khumbu glacier show a rapid increase in SAR  
435 backscatter magnitude for the higher elevation location, whereas backscatter time series extracted from within the  
436 elevation range of delayed melt offset show a gradual increase in radar backscatter. We interpret this gradual  
437 backscatter increase to be indicative of gradually decreasing liquid water content in the snowpack (or firn) as  
438 refreeze progresses from the glacier surface and into the depth of the percolation zone (*Fig. 7*) (Forster et al., 2014;  
439 Miège et al., 2016). This elevation range (~5,400-6,200 m a.s.l.) is similar to known elevation ranges of percolation  
440 zones on the Khumbu glacier as detailed in recent field work (Matthews et al., 2019; Matthews et al., 2020). SAR  
441 backscatter time series showing a gradual increase in backscatter within regions of known percolation suggest that a  
442 relationship between frozen percolation zone depth and the rate of C-band backscatter change across refreeze cycles.  
443 It has been shown that C-band backscatter gradually increases with frozen percolation zone depth and decreasing  
444 percolation zone wetness during a refreeze process (Ashcraft and Long, 2005).

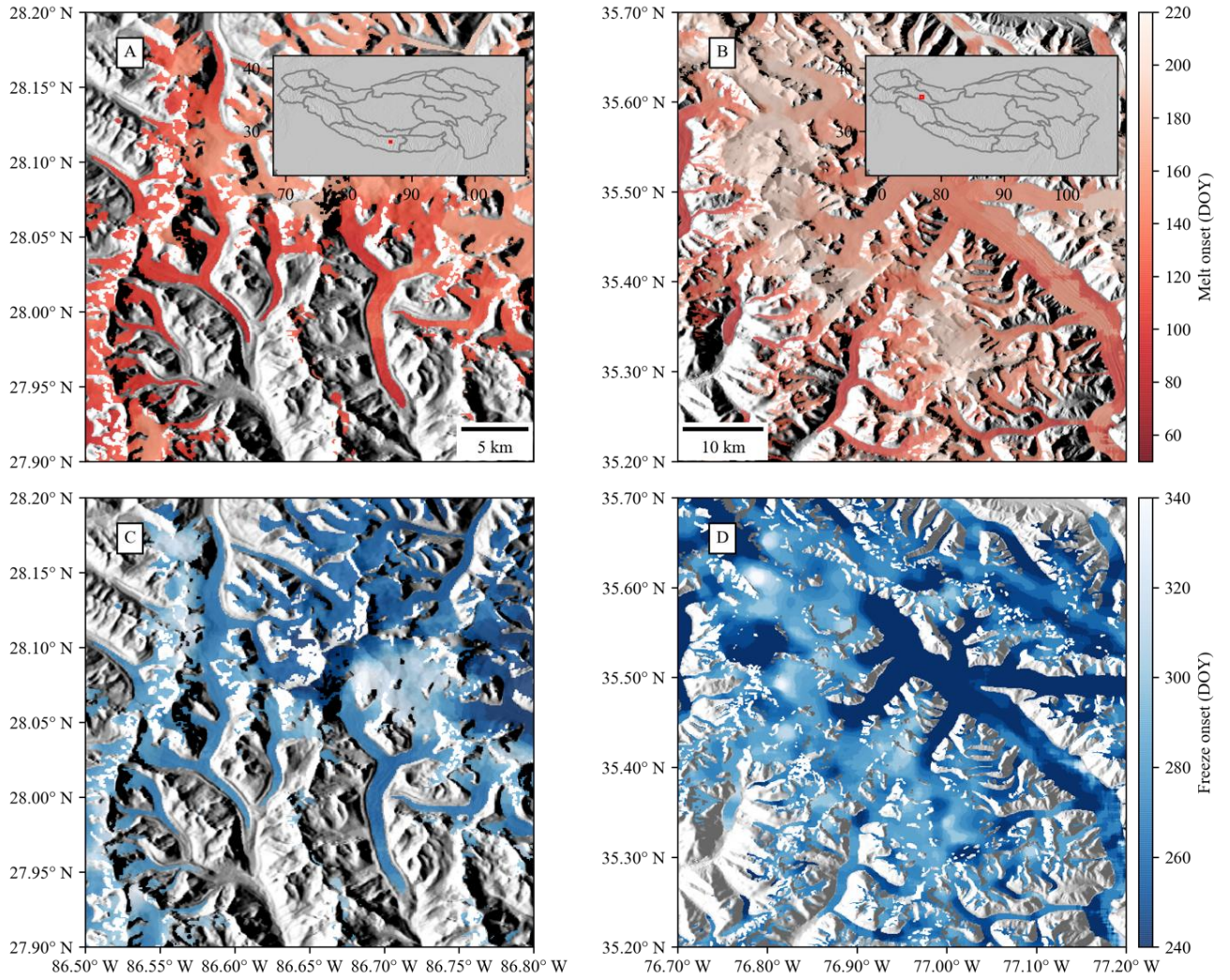


445

446 **Figure 7. (Top)** Refreeze timing over Khumbu glacier region of Mount Everest in the Central Himalaya. Red  
447 regions of freeze onset occur at mid-elevations, indicative of delayed refreeze due to meltwater retention in  
448 percolation zones. **(Bottom)** Sentinel-1 backscatter time series from two points on the Khumbu glacier, one within  
449 known elevations of glacier percolation facies (teal square, 6,000 m a.s.l.) and another point at elevations where  
450 temperatures likely do not exceed 0°C annually (pink triangle, 6,600 m a.s.l.).  
451

## 452 **4.2 Spatial Variability: Radar Scattering and Glacier Facies**

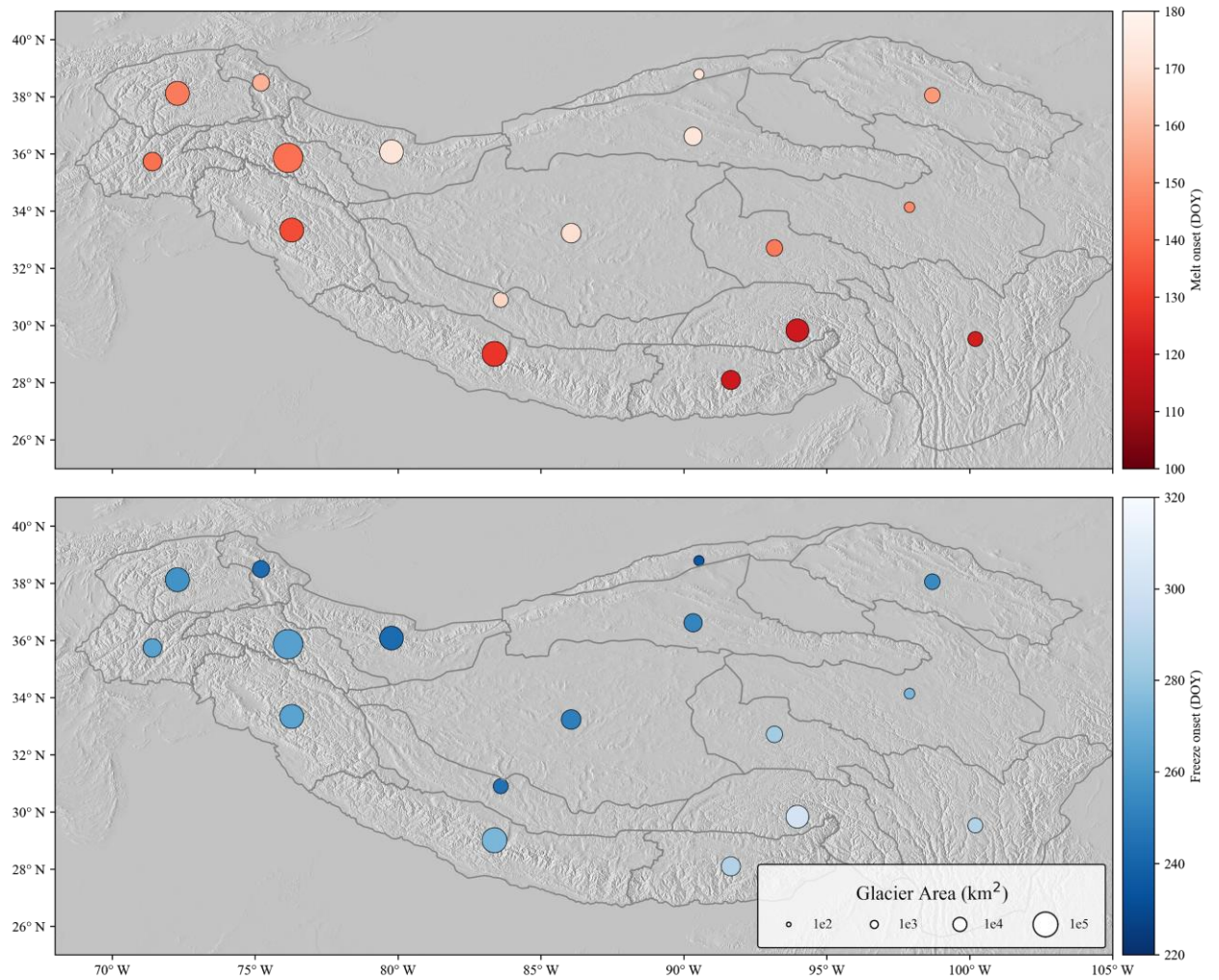
453 Imaging radar backscatter intensity, and response to surface melting, is linked with glacier facies (Ramage  
454 et al., 2000; Rau et al., 2000; Zhou and Zheng, 2017). Snow melting on the glacier surface produces a strong  
455 decrease in radar backscatter across all glacier facies. In the accumulation zone the refreeze signal is also  
456 pronounced as the dissipation of strongly absorbing wet snow at the surface is followed by volume scattering from  
457 deep snowpack and stratified ice layering. The scattering response to refreeze in the ablation zone is more complex  
458 and not well characterized. Here, supra-glacier features like crevasses, sun-cups, debris-cover, and other  
459 heterogeneities are likely to cause highly variable radar scattering mechanisms over short distances upon the  
460 disappearance of snow from the ablation surface. (Rott and Mätzler, 1987). We use the  $z$ -score metric to select areas  
461 where radar backscatter increases substantially during the refreeze process. However, since scattering response  
462 during the transition from wet snow will differ with various surface features (e.g. bare ice, debris and supra-glacier  
463 ponding) it is difficult to isolate the refreeze response. Average  $z$  is minimum in the HKH across the lowest  
464 elevation glacier surfaces (2,000m-4,000m a.s.l.) whereas  $z$  is maximum at unique elevation ranges within sub-  
465 regions (*Fig. 4, Supplementary Fig. S2*). Ablation zone surfaces (at lower elevations) do not exhibit the magnitude  
466 of backscatter intensity of percolation zones and therefore lower glaciated elevations show lesser seasonal contrast  
467 than higher elevations. These differences are also apparent in the spatial granularity of melt retrievals from the S1-  
468 SAR product, as shown in *Fig. 8*. Ablation zone surfaces on valley glaciers show spatial heterogeneity in MO  
469 indicative of supraglacial features, like debris cover, rather than randomly distributed noise. There exists uncertainty  
470 in the FO signal on glacier ablation surfaces that will require further investigation. In ablation areas with lower  
471 sensitivity to melting, we hypothesize that snow-off conditions result in increase of radar backscatter due to  
472 contributions to scattering from wet debris, bare ice, or other ablation surface heterogeneities related to rough  
473 surface scattering. For this reason, at lower elevations where annual air temperatures exceed 0°C (i.e. where  
474 temperature-elevation lapse rates hold), lapse rate estimates of elevation might be more robust estimates of FO using  
475 this approach. Overall, surface melting signals appear to be consistent with expectations of temperature lapse rates  
476 (i.e. earlier melting and later refreeze at lower elevations) across elevations where annual air temperatures likely  
477 exceed 0°C (<6,000 m a.s.l.). We have illustrated the spatial granularity of melt retrievals in *Fig. 8* in addition to  
478 average melt onset and offset by sub-region in *Fig. 9*.  
479



480  
 481  
 482  
 483  
 484  
 485

**Figure 8.** Melt retrievals averaged over the calendar years 2017-2019 in the Central Himalaya and Karakoram regions. **(A)** Mean melt onset (DOY) in the Central Himalaya. **(B)** Mean melt onset (DOY) over the Siachen glacier in the Karakoram region. **(C)** Mean melt offset (DOY) in the Central Himalaya. **(D)** Mean melt offset (DOY) over the Siachen glacier in the Karakoram region.



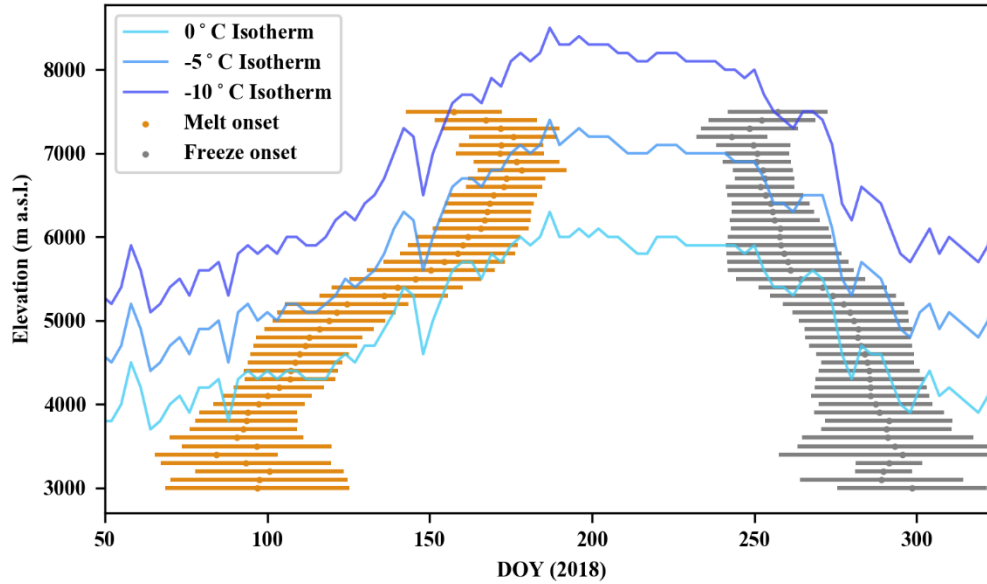


486  
 487  
 488  
 489  
 490  
 491  
 492  
 493  
 494  
 495  
 496  
 497  
 498  
 499  
 500  
 501  
 502

**Figure 9.** Melt onset (top) and freeze onset (bottom) averaged over 2017-2019 plotted over a SRTM 30m DEM hillshade (Farr, 2007). Melt retrievals are averaged across HiMAP glacio-climate sub-regions (Bolch et al., 2019a; Shean et al., 2020) and scaled by the mapped glacier area within each sub-region.

### 503 4.3 Considerations of Temperature-Elevation Lapse Rates

504



505  
506  
507  
508  
509  
510

**Figure 7.** Sentinel-1 SAR retrieved melt onset (orange) and freeze onset (gray), with spatial variability at  $\pm 1$  standard deviation, across the Central Himalaya region. The elevations of the 0°C, -5°C, and -10°C isotherms from 2018 are overlaid for comparison. Melt signals are recorded in excess of three months at elevations extending >1km above the maximum elevation of the 0°C isotherm, indicative of a sustained presence of liquid water within the snow matrix across these high elevation ranges.

511  
512  
513  
514  
515  
516  
517  
518  
519  
520  
521  
522  
523  
524  
525  
526  
527

We compare SAR retrievals of MO and FO to temperature-elevation lapse rates derived within a catchment in the Central Himalaya to investigate SAR retrievals alongside lapse-rate assumptions of glacier melt status; using methods and AWS data for the construction of lapse-rates from prior studies in the Langtang valley, Central Himalaya (Baral et al., 2014). In 2018, we observe that the average MO is found to follow the 0° and -5°C isotherms for elevations ~4,500 to 6,500m a.s.l. Below and above these elevations, and for FO, we find episodic melting events occurring over a range of elevations. This is especially apparent in the FO around day of year 270 where FO occurs within a roughly two week period across glaciers between 5,000m-7,500m a.s.l. MO and FO signals are retrieved on days and at elevations where lapse-rate derived temperatures do not exceed -10°C, which strengthens and expands recent *in situ* observations on glacier melt at the Khumbu glacier in the Mount Everest region showing incident shortwave radiation drives melt at these temperatures and elevations (Matthews et al., 2019). Here we observe that, even at these extreme elevations (>7,000m a.s.l.) melt signals persist for over three months on average across the Central Himalaya, which suggests that liquid water is retained at these high elevations across a seasonal melt cycle and may not be hydrologically negligible. In radar-derived observations there is a discrepancy between SAR and lapse-rate estimated melting records that occurs at elevations extending 1km above the maximum 0°C isotherms in the Central Himalaya. Glaciated areas in the Central Himalaya at elevations greater than 6,000m a.s.l. – the approximate maximum elevation of the 0°C isotherm for 2018 – account for 21.58% (2,453 km<sup>2</sup>) of total glaciated area within the region.

528

#### 529 **4.4 Melt Retrievals and Glacio-Climatic Sub-regions**

530 The three-year record of Sentinel-1 SAR retrievals of glacier melt status represent a baseline measurement  
531 for the HMA. The summary melt statistics are aggregated over HiMAP sub-regions in order to compare melt  
532 retrievals and sub-regional estimates of glacier mass wasting (Bolch, et al. 2019a; Shean, et al., 2020). Overall, the  
533 HMA sub-regions with the most rapid mass wasting between 2000-2010 tabulated in Shean, et al. (2019a) (Eastern  
534 Himalaya, Hengduan Shan, Nyainquntanglha) exhibit the greatest number of melt days on average in 2017-2019  
535 from Sentinel-1 retrievals. Sub-regions with slower mass wasting, in steady state, or with mass slight gain (Eastern  
536 Hindu Kush, Western Pamir, Karakoram, Tibetan Interior) show on average one month less of melt duration relative  
537 to regions with accelerated mass wasting. Interestingly, the Gangdise sub-region, with one of the higher post-2000  
538 rates of glacier wasting in the HKH, shows annual melt durations of less than three months on average, which  
539 appears more characteristic of western regions with slower mass wasting (i.e. Tibetan Interior Mountains). Although  
540 Sentinel-1 retrievals of glacier melt status for three calendar years does not make-up a climatic record, we observe  
541 that between 2017-2019 there was on average less duration of melting in regions where *in situ* data and climate  
542 models indicate that frozen winter precipitation contributes to glacier accumulation despite warming global climate  
543 (Karakoram, Hindu Kush, Eastern Pamir, Western Himalaya) (Kääb et al., 2015; Kapnick et al., 2014; Palazzi et al.,  
544 2013). We interpret shorter duration of annual melt days in the western regions of the HKH as a potential indicator  
545 of the “Karakoram Anomaly” reflected in the Sentinel-1 data record. Because the meteo-climatic drivers of the  
546 Karakoram Anomaly are still under debate (Farinotti et al., 2020), Sentinel-1 retrievals of melt duration may be  
547 useful for interrogating meteo-climatic drivers of heterogeneity in glacier wasting dynamics across the HKH.

#### 548 **5 Conclusion**

549 Synthetic aperture radar time series backscatter images and glacier extent maps derived from optical imagery  
550 have long been proposed to inform hydrologic and glaciologic research across the global cryosphere, however a  
551 harmonized dataset of glacier surface melt does not exist. We retrieve glacier surface melt timing and duration for  
552 the study years 2017-19 across the HKH region using time series C-band SAR from the Sentinel-1 A/B satellites and  
553 an inventory of 105,432 glaciers spanning 83,102 km<sup>2</sup> of ice-covered area. We quantify the magnitude of the  
554 seasonal melt signal by comparing mean summer and winter backscatter using a *z*-score metric and retrieve  
555 constraints on seasonal melt characteristics across all glaciated elevations of HKH at 90m spatial and 12-day  
556 temporal resolution. Melt conditions in surface energy balance models of glacier melt driven by *in situ*  
557 meteorological data from Mount Everest are constrained by Sentinel-1 SAR melt retrievals. Comparison of melt  
558 retrievals to temperature-elevation lapse rates calculated using two high-elevation meteorological stations in the  
559 Central Himalaya reveal that melt onset persists for over three months at elevations where extrapolated air  
560 temperature fields do not exceed -10°C. Melt is retrieved across all elevation ranges of HKH glaciers, which  
561 suggests that a dry snow accumulation zone in the HKH region does not exist. Meltwater retention is indicated  
562 within known glacier percolation zones on Mount Everest through signals of delayed refreeze. Delayed refreeze



563 occurs across the HKH at elevations with the greatest seasonal contrast in backscatter intensity, attributable to radar  
564 scattering in percolation facies. Melt signals persist for a greater portion of the year in regions known for rapid  
565 contemporary glacier wasting (i.e. Central and Eastern Himalaya sub-regions) whereas regions with stable glacier  
566 mass balance (i.e. Karakoram) exhibit a shorter duration of annual melt. We produce a geospatial data product of  
567 melt onset (DOY) and freeze onset (DOY) spanning glaciers of the HKH region at 90m spatial resolution for the  
568 calendar years 2017-2019 and plan to release annual updates to this dataset each calendar year across the mission  
569 duration of Sentinel-1. The methods presented in this study can provide the basis for an operational monitor of  
570 glacier surface melt dynamics and aid the development and assessment of surface energy balance models of glacier  
571 ablation across the global cryosphere.

## 572 **6 Acknowledgements**

573 This work was supported by funds provided to The City College of New York by the National Aeronautics and  
574 Space Administration Cryosphere Program's High Mountain Asia Team (HiMAT) program, under award number  
575 NNX16AQ83G. Portions of this work were conducted at the Jet Propulsion Laboratory, California Institute of  
576 Technology, under contract to the National Aeronautics and Space Administration.

## 577 **Author Contribution**

578 N. C. Steiner and K. C. McDonald devised the project and the main conceptual ideas. C. Scher developed and  
579 executed the 425 final methodological approach and authored the computer code. C.S contributed most of the  
580 writing to the manuscript with major contributions from N.C.S. K.C.M supervised the project and manuscript.  
581

## 582 **Competing Interest**

583 The authors declare no competing interests.

## 584 **Code and Data availability**

585 The code and data will be available on in the NASA Distributed Active Archive Center, the National Snow and Ice  
586 Data Center, as part of the High Mountain Asia Data archive.

## 587 **7 References**

588 Abdalati, W. and Steffen, K.: Greenland Ice Sheet melt extent: 1979-1999, *Journal of Geophysical Research:*  
589 *Atmospheres*, 106, 33983-33988, 2001.  
590  
591 Adam, S., Pietroniro, A., and Brugman, M. M.: Glacier snow line mapping using ERS-1 SAR imagery, *Remote*  
592 *Sensing of Environment*, 61, 46-54, 1997.

593  
594 Alexander, P., Tedesco, M., Koenig, L., and Fettweis, X.: Evaluating a regional climate model simulation of  
595 Greenland ice sheet snow and firn density for improved surface mass balance estimates, *Geophysical Research*  
596 *Letters*, 46, 12073-12082, 2019.  
597  
598 Anthwal, A., Joshi, V., Sharma, A., and Anthwal, S.: Retreat of Himalayan glaciers—indicator of climate change,  
599 *Nature and Science*, 4, 53-59, 2006.  
600  
601 Ashcraft, I. S. and Long, D. G.: Comparison of methods for melt detection over Greenland using active and passive  
602 microwave measurements, *International Journal of Remote Sensing*, 27, 2469-2488, 2007.  
603  
604 Ashcraft, I. S. and Long, D. G.: Differentiation between melt and freeze stages of the melt cycle using SSM/I  
605 channel ratios, *IEEE transactions on geoscience and remote sensing*, 43, 1317-1323, 2005.  
606  
607 Baghdadi, N., Gauthier, Y., and Bernier, M.: Capability of multitemporal ERS-1 SAR data for wet-snow mapping,  
608 *Remote sensing of environment*, 60, 174-186, 1997.  
609  
610 Bahr, D. B., Meier, M. F., and Peckham, S. D.: The physical basis of glacier volume-area scaling, *Journal of*  
611 *Geophysical Research: Solid Earth*, 102, 20355-20362, 1997.  
612  
613 Baral, P., Kayastha, R. B., Immerzeel, W. W., Pradhananga, N. S., Bhattarai, B. C., Shahi, S., Galos, S., Springer,  
614 C., Joshi, S. P., and Mool, P. K.: Preliminary results of mass-balance observations of Yala Glacier and analysis of  
615 temperature and precipitation gradients in Langtang Valley, Nepal, *Annals of glaciology*, 55, 9-14, 2014.  
616  
617 Bhattacharya, I., Jezek, K. C., Wang, L., and Liu, H.: Surface melt area variability of the Greenland ice sheet: 1979–  
618 2008, *Geophysical Research Letters*, 36, 2009.  
619  
620 Bindshadler, R., Jezek, K., and Crawford, J.: Glaciological investigations using the synthetic aperture radar  
621 imaging system, *Annals of Glaciology*, 9, 11-19, 1987.  
622  
623 Bogardi, J. J., Dudgeon, D., Lawford, R., Flinkerbusch, E., Meyn, A., Pahl-Wostl, C., Vielhauer, K., and  
624 Vörösmarty, C.: Water security for a planet under pressure: interconnected challenges of a changing world call for  
625 sustainable solutions, *Current Opinion in Environmental Sustainability*, 4, 35-43, 2012.  
626  
627 Bolch, T., Shea, J. M., Liu, S., Azam, F. M., Gao, Y., Gruber, S., Immerzeel, W. W., Kulkarni, A., Li, H., and Tahir,  
628 A. A.: Status and change of the cryosphere in the Extended Hindu Kush Himalaya Region. In: *The Hindu Kush*  
629 *Himalaya Assessment*, Springer, 2019a.  
630  
631 Bolch, T., Kulkarni, A., Käab, A., Huggel, C., Paul, F., Cogley, J. G., Frey, H., Kargel, J. S., Fujita, K., and Scheel,  
632 M. J. S.: The state and fate of Himalayan glaciers, 336, 310-314, 2012.  
633  
634 Bolch, T., Bhattacharya, A., King, O., and Allen, S.: Characteristics and changes of glaciers, rock glaciers and  
635 glacial lakes in High Mountain Asia since the 1960s, 2019b.  
636  
637 Brangers, I., Lievens, H., Miège, C., Demuzere, M., Brucker, L., and De Lannoy, G.: Sentinel-1 detects firn aquifers  
638 in the Greenland Ice Sheet, *Geophysical Research Letters*.  
639  
640 Brock, B. W., Willis, I. C., and Sharp, M. J.: Measurement and parameterization of aerodynamic roughness length  
641 variations at Haut Glacier d’Arolla, Switzerland, *Journal of Glaciology*, 52, 281-297, 2006.  
642  
643 Brown, L. E., Hannah, D. M., and Milner, A. M.: Vulnerability of alpine stream biodiversity to shrinking glaciers  
644 and snowpacks, *Global Change Biology*, 13, 958-966, 2007.  
645  
646 Brun, F., Berthier, E., Wagnon, P., Kaab, A., and Treichler, D.: A spatially resolved estimate of High Mountain Asia  
647 glacier mass balances, 2000-2016, *Nat Geosci*, 10, 668-673, 2017.  
648

649 Carrivick, J. L. and Tweed, F. S.: A global assessment of the societal impacts of glacier outburst floods, *Global and*  
650 *Planetary Change*, 144, 1-16, 2016.

651

652 Engeset, R., Kohler, J., Melvold, K., and Lundén, B.: Change detection and monitoring of glacier mass balance and  
653 facies using ERS SAR winter images over Svalbard, *International Journal of Remote Sensing*, 23, 2023-2050, 2002.  
654 ESA: <https://sentinel.esa.int/web/sentinel/user-guides/sentinel-1-sar/acquisition-modes/interferometric-wide-swath>,  
655 last access: February 13, 2020.

656

657 Farinotti, D., Immerzeel, W. W., de Kok, R. J., Quincey, D. J., and Dehecq, A.: Manifestations and mechanisms of  
658 the Karakoram glacier Anomaly, *Nature Geoscience*, 13, 8-16, 2020.

659

660 Farr, T. G., Rosen, P.A., Caro, E., Crippen, R., Duren, R., Hensley, S., Kobrick, M., Paller, M., Rodriguez, E., Roth,  
661 L., Seal, D., Shaffer, S., Shimada, J., Umland, J., Werner, M., Oskin, M., Burbank, D., and Alsdorf, D.E.: The  
662 shuttle radar topography mission: *Reviews of Geophysics*, v. 45, no. 2, RG2004, at  
663 <https://doi.org/10.1029/2005RG000183>, *Reviews of Geophysics*, 45, 2007.

664

665 Fischer, G., Jäger, M., Papathanassiou, K. P., and Hajnsek, I.: Modeling the Vertical Backscattering Distribution in  
666 the Percolation Zone of the Greenland Ice Sheet with SAR Tomography, *IEEE Journal of Selected Topics in*  
667 *Applied Earth Observations and Remote Sensing*, 12, 4389-4405, 2019.

668

669 Fujita, K. and Nuimura, T.: Spatially heterogeneous wastage of Himalayan glaciers, *Proc Natl Acad Sci U S A*, 108,  
670 14011-14014, 2011.

671

672 Gardelle, J., Berthier, E., and Arnaud, Y.: Slight mass gain of Karakoram glaciers in the early twenty-first century,  
673 *Nature geoscience*, 5, 322, 2012.

674

675 Google: Sentinel-1 Preprocessing, last access: November 30, 2020 2020.

676

677 Gorelick, N., Hancher, M., Dixon, M., Ilyushchenko, S., Thau, D., and Moore, R. J. R. S. o. E.: Google Earth  
678 Engine: Planetary-scale geospatial analysis for everyone, 202, 18-27, 2017.

679

680 Hallikainen, M., Ulaby, F., and Abdelrazik, M.: Dielectric properties of snow in the 3 to 37 GHz range, *IEEE*  
681 *transactions on Antennas and Propagation*, 34, 1329-1340, 1986.

682

683 Huang, L., Li, Z., Tian, B.-S., Chen, Q., Liu, J.-L., and Zhang, R.: Classification and snow line detection for glacial  
684 areas using the polarimetric SAR image, *Remote Sensing of Environment*, 115, 1721-1732, 2011.

685

686 Huang, W., DeVries, B., Huang, C., Lang, M., Jones, J., Creed, I., and Carroll, M.: Automated Extraction of Surface  
687 Water Extent from Sentinel-1 Data, *Remote Sensing*, 10, 2018.

688

689 ICIMOD: Outline Boundary of Hindu Kush Himalayan (HKH) Region. ICIMOD (Ed.), ICIMOD.

690 Jacobsen, D., Milner, A. M., Brown, L. E., and Dangles, O.: Biodiversity under threat in glacier-fed river systems,  
691 *Nature Climate Change*, 2, 361, 2012.

692

693 Jezek, K. C., Gogineni, P., and Shanableh, M.: Radar measurements of melt zones on the Greenland ice sheet,  
694 *Geophysical Research Letters*, 21, 33-36, 1994.

695

696 Kääh, A., Treichler, D., Nuth, C., and Berthier, E.: Brief Communication: Contending estimates of 2003–2008  
697 glacier mass balance over the Pamir–Karakoram–Himalaya, *Cryosphere*, 9, 2015.

698

699 Kapnick, S. B., Delworth, T. L., Ashfaq, M., Malyshev, S., and Milly, P. C.: Snowfall less sensitive to warming in  
700 Karakoram than in Himalayas due to a unique seasonal cycle, *Nature Geoscience*, 7, 834, 2014.

701 Kayastha, R. B., Steiner, N., Kayastha, R., Mishra, S. K., and McDonald, K.: Comparative study of hydrology and  
702 icemelt in three Nepal river basins using the glacio-hydrological degree-day model (GDM) and observations from  
703 the Advance Scatterometer (ASCAT), *FrEaS*, 7, 354, 2019.

704

705 Kendra, J. R., Sarabandi, K., Ulaby, F. T. J. I. T. o. G., and Sensing, R.: Radar measurements of snow: Experiment  
706 and analysis, 36, 864-879, 1998.  
707

708 Koskinen, J. T., Pulliainen, J. T., and Hallikainen, M. T.: The use of ERS-1 SAR data in snow melt monitoring,  
709 IEEE Transactions on geoscience and remote sensing, 35, 601-610, 1997.  
710

711 Lau, W. K., Kim, M.-K., Kim, K.-M., and Lee, W.-S.: Enhanced surface warming and accelerated snow melt in the  
712 Himalayas and Tibetan Plateau induced by absorbing aerosols, Environmental Research Letters, 5, 025204, 2010.  
713

714 Lievens, H., Demuzere, M., Marshall, H.-P., Reichle, R. H., Brucker, L., Brangers, I., de Rosnay, P., Dumont, M.,  
715 Giroto, M., and Immerzeel, W. W.: Snow depth variability in the Northern Hemisphere mountains observed from  
716 space, Nature communications, 10, 1-12, 2019.  
717

718 Litt, M., Shea, J., Wagnon, P., Steiner, J., Koch, I., Stigter, E., and Immerzeel, W.: Glacier ablation and temperature  
719 indexed melt models in the Nepalese Himalaya, Scientific reports, 9, 5264, 2019.  
720

721 Lund, J., Forster, R. R., Rupper, S. B., Marshall, H., Deeb, E. J., and Hashmi, M. Z. U. R.: Mapping snowmelt  
722 progression in the Upper Indus Basin with synthetic aperture radar, Frontiers in Earth Science, 7, 318, 2019.  
723 Margulis, S. A., Liu, Y., and Baldo, E.: A joint Landsat-and MODIS-based reanalysis approach for midlatitude  
724 montane seasonal snow characterization, Frontiers in Earth Science, 7, 272, 2019.  
725

726 Matthews, T., Perry, B., Aryal, D., Shrestha, D., and Khadka, A.: New Heights in Glacier-Climature Research: Initial  
727 Insights From the Highest Weather Stations on Earth, 2019.  
728

729 Matthews, T., Perry, L. B., Koch, I., Aryal, D., Khadka, A., Shrestha, D., Abernathy, K., Elmore, A., Seimon, A.,  
730 and Tait, A.: Going to Extremes: Installing the World's Highest Weather Stations on Mount Everest, B Am  
731 Meteorol Soc, 2020. 2020.  
732

733 Matzler, C.: Microwave properties of ice and snow. In: Solar System Ices, Springer, 1998.  
734

735 Miles, K. E., Hubbard, B., Quincey, D. J., Miles, E. S., Sherpa, T. C., Rowan, A. V., and Doyle, S. H.: Polythermal  
736 structure of a Himalayan debris-covered glacier revealed by borehole thermometry, Scientific reports, 8, 1-9, 2018.  
737

738 Milner, A. M., Khamis, K., Battin, T. J., Brittain, J. E., Barrand, N. E., Fureder, L., Cauvy-Fraunie, S., Gislason, G.  
739 M., Jacobsen, D., Hannah, D. M., Hodson, A. J., Hood, E., Lencioni, V., Olafsson, J. S., Robinson, C. T., Tranter,  
740 M., and Brown, L. E.: Glacier shrinkage driving global changes in downstream systems, Proc Natl Acad Sci U S A,  
741 114, 9770-9778, 2017.  
742

743 Nagler, T. and Rott, H.: Retrieval of wet snow by means of multitemporal SAR data, IEEE Transactions on  
744 Geoscience and Remote Sensing, 38, 754-765, 2000.  
745

746 Nagler, T., Rott, H., Ripper, E., Bippus, G., and Hetzenecker, M.: Advancements for Snowmelt Monitoring by  
747 Means of Sentinel-1 SAR, Remote Sensing, 8, 348, 2016.  
748

749 Nuimura, T., Sakai, A., Taniguchi, K., Nagai, H., Lamsal, D., Tsutaki, S., Kozawa, A., Hoshina, Y., Takenaka, S.,  
750 and Omiya, S.: The gamdam glacier inventory: a quality-controlled inventory of Asian glaciers, Cryosphere, 9,  
751 2015.  
752

753 Oza, S., Singh, R., Vyas, N., and Sarkar, A.: Study of inter-annual variations in surface melting over Amery Ice  
754 Shelf, East Antarctica, using space-borne scatterometer data, Journal of earth system science, 120, 329-336, 2011.  
755

756 Palazzi, E., Von Hardenberg, J., and Provenzale, A.: Precipitation in the Hindu-Kush Karakoram Himalaya:  
757 observations and future scenarios, Journal of Geophysical Research: Atmospheres, 118, 85-100, 2013.  
758

759 Paterson, W. S. B.: The physics of glaciers, Elsevier, 2016.  
760

761 Pritchard, D. M., Forsythe, N., O'Donnell, G., Fowler, H. J., and Rutter, N.: Multi-physics ensemble snow modelling  
762 in the western Himalaya, *The Cryosphere*, 2020. 2020.  
763

764 Ramage, J. M., Isacks, B. L., and Miller, M. M.: Radar glacier zones in southeast Alaska, USA: field and satellite  
765 observations, *Journal of Glaciology*, 46, 287-296, 2000.  
766

767 Rau, F., Braun, M., Friedrich, M., Weber, F., and Goßmann, H.: Radar glacier zones and their boundaries as  
768 indicators of glacier mass balance and climatic variability, 2000, 317-327.  
769

770 Rott, H. and Mätzler, C.: Possibilities and limits of synthetic aperture radar for snow and glacier surveying, *Annals*  
771 *of Glaciology*, 9, 195-199, 1987.  
772

773 Sakai, A.: Brief communication: Updated GAMDAM glacier inventory over high-mountain Asia, *The Cryosphere*,  
774 13, 2043-2049, 2019.  
775

776 Scott, C. A., Zhang, F., Mukherji, A., Immerzeel, W., Mustafa, D., and Bharati, L.: Water in the Hindu Kush  
777 Himalaya. In: *The Hindu Kush Himalaya Assessment*, Springer, 2019.  
778

779 Shea, J.: Meteorological data from Yala Base Camp automatic weather station. ICIMOD (Ed.), 2016.  
780

781 Shean, D. E., Bhushan, S., Montesano, P., Rounce, D. R., Arendt, A., and Osmanoglu, B.: A Systematic, Regional  
782 Assessment of High Mountain Asia Glacier Mass Balance, *Frontiers in Earth Science*, 7, 2020.  
783

784 Shi, J. and Dozier, J.: Inferring snow wetness using C-band data from SIR-C's polarimetric synthetic aperture radar,  
785 *IEEE transactions on geoscience and remote sensing*, 33, 905-914, 1995.  
786

787 Shi, J., Dozier, J., and Rott, H.: Snow mapping in alpine regions with synthetic aperture radar, *IEEE Transactions on*  
788 *Geoscience and Remote Sensing*, 32, 152-158, 1994.  
789

790 Steiner, N. and Tedesco, M.: A wavelet melt detection algorithm applied to enhanced-resolution scatterometer data  
791 over Antarctica (2000–2009), *The Cryosphere*, 8, 25-40, 2014.  
792

793 Trusel, L. D., Frey, K. E., and Das, S. B.: Antarctic surface melting dynamics: Enhanced perspectives from radar  
794 scatterometer data, *Journal of Geophysical Research: Earth Surface*, 117, 2012.  
795

796 Winebrenner, D. P., Nelson, E. D., Colony, R., and West, R. D.: Observation of melt onset on multiyear Arctic sea  
797 ice using the ERS 1 synthetic aperture radar, *Journal of Geophysical Research*, 99, 1994.  
798

799 Winsvold, S., Kääh, A., Nuth, C., Andreassen, L. M., Van Pelt, W., and Schellenberger, T.: Using SAR data time-  
800 series for regional glacier mapping, *The Cryosphere*, 12, 867-890, 2018.  
801

802 Wiscombe, W. J. and Warren, S. G. J. J. o. t. A. S.: A model for the spectral albedo of snow. I: Pure snow, 37, 2712-  
803 2733, 1980.  
804

805 Wood, L. R., Neumann, K., Nicholson, K. N., Bird, B. W., Dowling, C. B., and Sharma, S.: Melting Himalayan  
806 Glaciers Threaten Domestic Water Resources in the Mount Everest Region, Nepal, *Frontiers in Earth Science*, 8,  
807 2020.  
808

809 Yao, T., Thompson, L. G., Mosbrugger, V., Zhang, F., Ma, Y., Luo, T., Xu, B., Yang, X., Joswiak, D. R., and  
810 Wang, W.: Third pole environment (TPE), *Environmental Development*, 3, 52-64, 2012.  
811

812 Zemp, M., Haeberli, W., Hoelzle, M., and Paul, F.: Alpine glaciers to disappear within decades?, *Geophysical*  
813 *Research Letters*, 33, 2006.  
814

815 Zemp, M., Huss, M., Thibert, E., Eckert, N., McNabb, R., Huber, J., Barandun, M., Machguth, H., Nussbaumer, S.  
816 U., and Gärtner-Roer, I.: Global glacier mass changes and their contributions to sea-level rise from 1961 to 2016,  
817 Nature, 568, 382-386, 2019.  
818  
819 Zhou, C. and Zheng, L.: Mapping Radar Glacier Zones and Dry Snow Line in the Antarctic Peninsula Using  
820 Sentinel-1 Images, Remote Sensing, 9, 2017.  
821